

Interplay of crystal thickness and in-plane anisotropy and evolution of quasi-one dimensional electronic character in ReSe₂

Lewis S. Hart,¹ Surani M. Gunasekera,¹ Marcin Mucha-Kruczyński,¹ James L. Webb,² José Avila,³ María C. Asensio,⁴ and Daniel Wolverson^{1,*}

¹*Centre for Nanoscience and Nanotechnology and Department of Physics, University of Bath, Bath BA2 7AY, United Kingdom*

²*Center for Macroscopic Quantum States (bigQ), Department of Physics, Technical University of Denmark, Kgs. Lyngby, Denmark*

³*Synchrotron SOLEIL, Saint Aubin and Université Paris-Saclay, BP 48 91192 Gif-sur-Yvette, France*

⁴*Madrid Institute of Materials Science (ICMM),*

Spanish Scientific Research Council (CSIC) and CSIC associated unit MATINÉE (ICMM and Institute of Materials Science of Valencia University, ICMUV) Cantoblanco, E-28049 Madrid, Spain

We study the valence band structure of ReSe₂ crystals with varying thickness down to a single layer using nanoscale angle-resolved photoemission spectroscopy and density functional theory. The width of the top valence band in the direction perpendicular to the rhenium chains decreases with decreasing number of layers, from ~ 200 meV for the bulk to ~ 80 meV for monolayer. This demonstrates increase of in-plane anisotropy induced by changes in the interlayer coupling and suggests progressively more one-dimensional character of electronic states in few-layer rhenium dichalcogenides.

I. INTRODUCTION

The transition metal dichalcogenides (TMDs) present a fascinating diversity of behaviour including: thickness-driven indirect-to-direct semiconducting band gap transitions; metals; magnetic phases; charge density wave materials; superconductors, and materials with topological surface states [1]. They are readily combined in vertical heterostructures with atomically precise interfaces and offer unprecedented degrees of built-in control over their optical [2] and electronic [3] properties via novel means such as variation of the heterostructure twist angle [4] and more conventional methods, such as strain [5] or electrostatic gating [6].

Within the TMD family, ReSe₂ and ReS₂ are distinguished by in-plane anisotropy due to a Jahn-Teller distortion which breaks the 120° in-plane rotational symmetry common to two-dimensional crystals and leads to the formation of rhenium chains [7]. It also causes out-of-plane buckling of chalcogens which results in lack of atomic registry between consecutive layers and contributes to weakening of the interlayer interaction. The in-plane anisotropy and weak interlayer coupling impact many of the properties of rhenium dichalcogenides, from charge transport and optical absorption [8] to high catalytic activity as shown in solar water splitting [9–11].

One of the most intriguing fundamental questions associated with layered materials is the understanding of the changes occurring as they are thinned down from three-dimensional bulk to single, two-dimensional atomic planes. In many materials such as 2H semiconducting TMDs [12–14], post-transition-metal monochalcogenides [15–17] and black phosphorus [18], parts of the valence

band are formed by orbitals extending significantly in the out-of-plane direction (e.g., p_z or d_{z^2}) which are strongly affected by the presence of neighbouring layers and interlayer coupling. As a result, the shape of the valence band depends sensitively on the number of layers in the crystal leading to, for example, indirect-to-direct band gap transitions [12–14]. In contrast, in rhenium TMDs, it is rhenium d_{xy} and $d_{x^2-y^2}$ rather than d_{z^2} or chalcogen p_z orbitals that form the top of the valence band [19, 20]. As these are the orbitals participating in the Jahn-Teller distortion, this poses the question of whether the in-plane anisotropy of the valence band could be influenced by tuning the interlayer interaction.

Here, we use nanoscale angle-resolved photoemission spectroscopy (nano-ARPES) supported by density functional theory calculations to study the interplay between the in-plane anisotropy and crystal thickness in the electronic band structure of ReSe₂, from bulk down to the monolayer limit. We show that, as previously argued for this compound [20], the position of the valence band maximum does not change with the number of layers. However, we observe a decrease of the width of the top valence band in the direction perpendicular to the rhenium chains with decreasing thickness, indicating the increasing decoupling of rhenium chains and the growing one-dimensional character of the electronic states.

II. METHODS

Sample preparation, characterisation details, and complete raw data are given in the Supplemental Material (SM) [21], Figs S1-S8. Nano-ARPES data were obtained at the ANTARES beamline of the SOLEIL synchrotron, Paris, which is equipped with a zone plate allowing a spot size of 120 nm, an angular resolution of $\sim 0.2^\circ$ and

* d.wolverson@bath.ac.uk

an energy resolution of ~ 10 meV. The high spatial resolution allows one to map the photoemission signal as a function of position with sub-micron resolution and thus to select flakes of different thickness. In this work, photon energies of 100 eV were used since the performance of the zone plate is optimal at this energy; the photoionisation cross-sections of Re $5d$ and Se $4p$ at 100 eV are comparable and are of order 0.1 to 0.2 Mbarn [22]. For the bulk flakes, this photon energy probes states with in-plane momenta lying in a plane near the Z point at the top of the Brillouin zone [23]. The sample cleaning process (see SM) resulted in layers which showed atomically clean and flat regions between the bubbles of trapped contaminants; no drift due to charging effects was observed. Raman spectroscopy, core-level nanoscale scanning photoemission microscopy (nano-XPS) and atomic force microscopy (AFM) were used as characterization tools.

Valence band structures were calculated using first principles plane wave, pseudopotential-based methods within density functional theory (DFT) as implemented in the Quantum Espresso package [24]. Both local density (LDA) and generalised gradient (GGA) approximations for the exchange-correlation functionals were used with the projector augmented wave (PAW) method [25, 26] being used in all cases. The valence of Re was taken as 15 (configuration $5s^25p^65d^56s^2$). $8 \times 8 \times 1$ Monkhorst-Pack [27] k -point meshes were used for monolayers and bilayers (12 and 24 atoms per unit cell respectively), and $6 \times 6 \times 6$ were used for the bulk (12 atoms). Kinetic energy cutoffs were, typically, > 800 eV. More computational details are given elsewhere [28, 29] where results using scalar- and fully-relativistic pseudopotentials are compared. Here, scalar-relativistic pseudopotentials were chosen so that wavefunction projections onto atomic states classified only by orbital angular momentum (i.e. without spin) could be conveniently obtained. Since ReSe₂ maintains inversion symmetry from bulk to monolayer, no spin-orbit splitting is expected at any point in the Brillouin zone for any layer thickness. Comparisons of calculated 1L bandstructures with and without spin-orbit coupling (SOC) have already been reported and the features of interest here are still present when SOC is included [28, 30, 31]. Representative calculations using fully-relativistic projector augmented wave (PAW) pseudopotentials are shown in Figure S7 in the SM for monolayer and bulk cases.

III. RESULTS

A. Characterization of atomically thin ReSe₂

Studying the dependence of the physical properties of layered materials as a function of their thickness requires samples with well-established layer numbers down to one monolayer. This task is more challenging than usual for the rhenium-based TMDs since, to enable comparisons

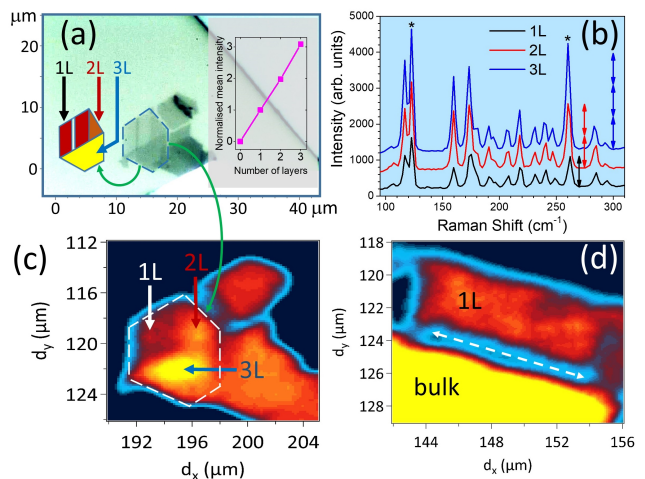


FIG. 1. Structure of the samples investigated. (a) Optical microscopy image of a few-layer ReSe₂ flake on an HOPG platform with the region of interest bounded by the dashed blue border; the sketch of this (on the left) identifies mono-, bi- and tri-layer areas (marked 1L, 2L 3L respectively) and the inset shows the dependence of the Raman intensity (averaged over two prominent peaks) on the number of layers; (b) micro-Raman spectra of the regions of the sample shown in (a), with asterisks indicating the two peaks used to calculate the mean intensity. A vertical shift has been applied for clarity; (c) nano-XPS map of the intensity of the Re $4f$ core levels (binding energy 40-44 eV) of the sample shown in (a) with the same region of interest indicated by the white dashed line; (d) nano-XPS intensity map of Re $4f$ core levels for a second sample with large monolayer and bulk-like regions; the dashed arrow shows a cleavage direction of this flake.

between different flakes, their crystallographic orientations must be established including, possibly, their vertical orientation [32, 33] as turning a flake upside-down is not a symmetry operation for ReSe₂. We have overcome this problem by exfoliating large flakes which contain regions of different thicknesses as shown in Fig. 1. Figure 1(a) shows an optical micrograph of a sample whose leftmost flake contains monolayer (1L), bilayer (2L) and trilayer (3L) regions, identified on the sketch to the left of the flake. All the regions derive from the same parent crystal and have preserved the same orientation as implied by the visible cleavage edges [34] at $\sim 60^\circ$ and $\sim 120^\circ$ and as confirmed rigorously by the Raman spectra of Fig. 1(b). Any significant rotation of one region with respect to the others would result in changes in the relative intensities of the different peaks within the spectrum due to the pronounced in-plane anisotropy of ReSe₂ [28, 32, 33, 35]. We confirmed layer numbers by four independent means: Raman spectroscopy, scanning photoemission microscopy, AFM and nano-ARPES (AFM images and line scans for all samples are shown in Figures S1 and S2 of the SM [21]). AFM step height measurements gave a monolayer thickness of $d \sim 0.60$ to 0.67 nm, comparable to the interlayer lattice parameter $c = 0.6702$ nm

[7, 36] (note, the crystallographic c axis in ReSe_2 is tilted away from the normal to the layer). The thicknesses of the 2L and 3L regions were likewise confirmed by AFM, Figure S2. Moreover, the Raman intensity from these regions scales linearly with the number of layers. This is best seen by looking at two Raman bands marked with asterisks in Figure 1(b) which dominate the spectrum and do not overlap strongly with other spectral features – vertical arrows next to the peaks clearly indicate the scaling. We also fit and average areas of these peaks following subtraction of a small background and present the results in the inset of panel (a). Since the silicon substrate does not have a thick oxide layer, and since the ReSe_2 layers were placed on a HOPG flake on the substrate, there is no modulation of the Raman intensity due to interference effects [28, 37]. The shifts in zone centre phonon frequencies with the number of layers are smaller for ReSe_2 and ReS_2 than for most TMDs [28, 38] so that, here, interference-free Raman intensities are more reliable than Raman peak shifts for determination of layer thicknesses. However, the measured Raman peak positions support our thickness assignments: the bulk modes at 283.6 and 260.5 cm^{-1} show a small shift to 285.2 and 263.0 cm^{-1} in the monolayer sample, in agreement with previous experimental and computational results [30].

Figures 1(c) and (d) show maps of the photoemission intensity from the Re $4f$ core levels (binding energy 40–44 eV) from the sample of Fig. 1(a) and one other sample containing monolayer and bulk regions with the same orientation. These maps were recorded primarily to locate the different regions for the ARPES experiments. Interestingly, the contrast in photoelectron count from 1L to 3L regions reflects the layer thicknesses. The core level photoemission intensity need not necessarily depend linearly on the number of ReSe_2 layers, but in principle it could be determined quantitatively by using X-ray photoelectron spectroscopy tools [39]. As Figs. 1(c) and (d) show, discrimination between regions differing by one layer is possible and this mapping correlates with the Raman data. Imaging based on possible shifts in the *energy* of the Re $4f$ core levels [40], on the other hand, did not produce any contrast between the different regions.

B. ARPES results from atomically thin ReSe_2

Because ReSe_2 possesses only inversion symmetry, the Brillouin zone of the monolayer is a distorted regular hexagon and the K and M points form three non-equivalent pairs (K_1, K_2, K_3 , M_1, M_2, M_3 and their inversion equivalents). In this work, we consider only dispersions in two key directions: along, and normal to, the Re chains, for simplicity labeled $\Gamma - K$ and $\Gamma - M$ respectively; see Fig. 2(a) for the indication of these directions in the real and reciprocal spaces and (b) for comparison of the bulk and two-dimensional Brillouin zones of ReSe_2 (the latter is a projection of the former along the reciprocal space c^* axis). These special directions cor-

respond to, for example, the polarization directions of the two band edge excitons in ReSe_2 [41–43] and were identified as the directions of maximum and minimum dispersion in the studies of bulk material [23, 44]. We present the measured valence band dispersions for the monolayer (1L) flake shown in Fig. 1(d) in Fig. 2(c,e) for $\Gamma - M$ and (d,f) for $\Gamma - K$. The right-hand panels in (c) and (d) show second derivatives with respect to energy of the data in the left, and in (e) and (f) we show expanded views of the same data and its second derivatives close to the valence band maximum (within $\sim 2\text{eV}$). The extraordinarily flat nature of the top of the valence band in the $\Gamma - M$ direction is striking and is the main result of this work. As we show later, this is very different to the bulk valence band structure. By contrast, the top valence band remains dispersive in the near-orthogonal direction $\Gamma - K$, Fig. 2(d,f). Because second derivatives can occasionally generate spurious features, we have examined the energy distribution curves (EDCs) which are the raw data for Fig. 2, directly. Figure S3 of the SM shows these EDCs in the $\Gamma - M$ and $\Gamma - K$ directions and confirms the flatness of the band along $\Gamma - M$ while the $\Gamma - K$ direction shows significant dispersion.

One more prominent feature of the 1L ReSe_2 valence band structure is the locally flat band centred at Γ at about 1 eV below the valence band edge (at a binding energy of ~ 2 eV) which yields a particularly high photoemission intensity. This feature was shown to correspond to the valence band formed predominantly by the out-of-plane Re d_{z^2} and Se p_z orbitals [20]. Figure 2 also shows the valence bands of the highly oriented pyrolytic graphite (HOPG) substrate on which the ReSe_2 flakes were placed. The observation of the Γ point of graphite (at $k_{\parallel} = 0$) usefully confirms the experimental location of the first Brillouin zone and Γ point of the ReSe_2 flakes and, as a result of the relatively large unit cell of ReSe_2 , the accessible momentum range allows us to sample almost two complete Brillouin zones in the $\Gamma - M$ direction. The data of Figure 2 show no evidence for hybridization or appreciable opening of gaps at the binding energy and momentum values where the bands of ReSe_2 and HOPG intersect. These results contrast with recent reported findings of strong coupling to graphene for TMDs such as WSe_2 [45] and MoS_2 [46] though, in those studies, the flakes also had graphene capping layers which the present samples did not.

C. Evolution of the valence band with the number of layers

Following the discussion of the ARPES of the monolayer region shown in Fig. 1(d), we move to the flake presented in Fig. 1(a) and (c). Between the two samples, we can not only test the reproducibility of the 1L results of Fig. 2 as well as those for the bulk, but also study the evolution of the valence band states as a function of crystal thickness. In Fig. 3, we show photointensity

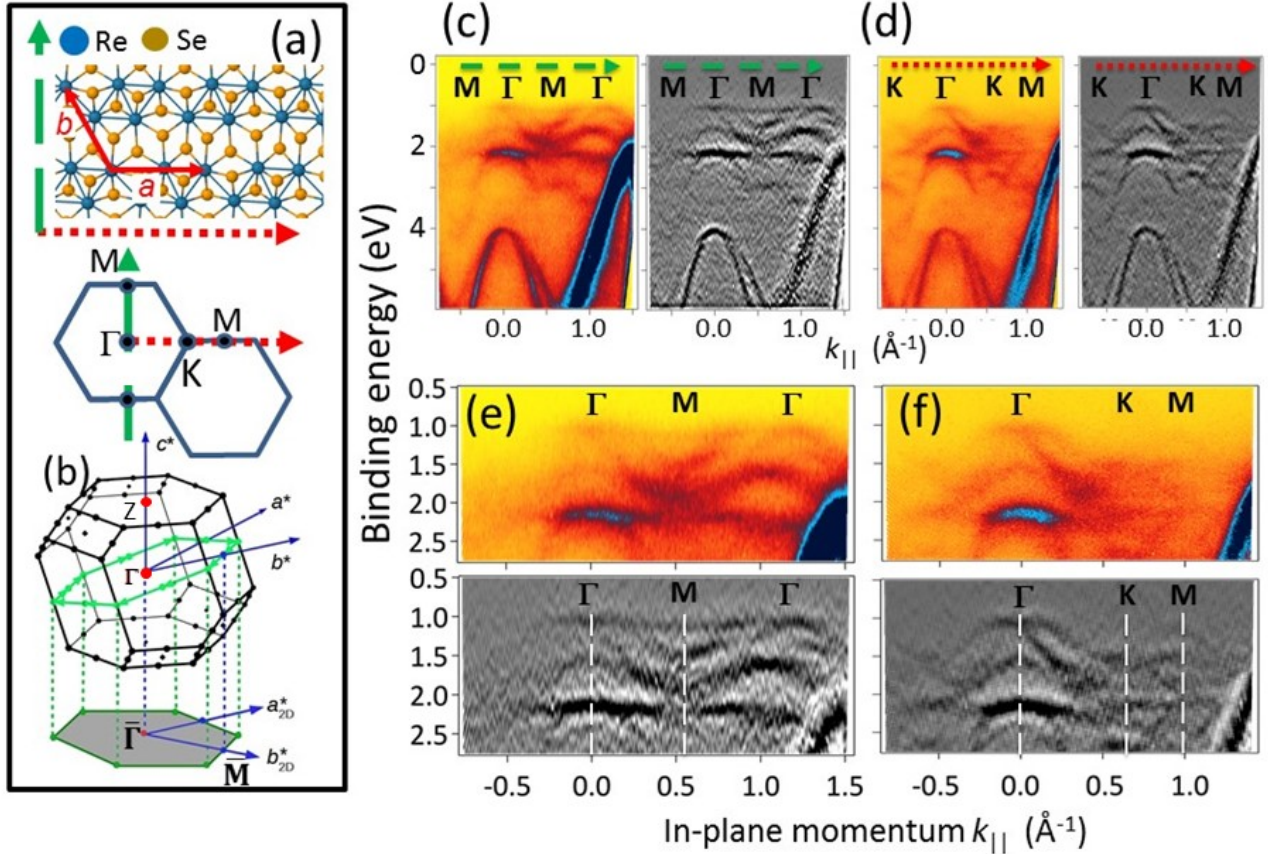


FIG. 2. Valence bands of monolayer ReSe₂. (a) Crystal structure (top) and reciprocal lattice of monolayer ReSe₂. Solid red arrows indicate in-plane lattice vectors a and b ; the rhenium ‘chains’ are oriented along a . In-plane directions $\Gamma - K$ (red dotted arrow) and $\Gamma - M$ (green dashed arrow) are displayed in relation to the top view of the real space layer plane. (b) First Brillouin zone of bulk ReSe₂ with reciprocal lattice vectors a^* , b^* and c^* and their projections onto the 2D layer plane; Γ and Z points are also shown. (c) Left: photoemission intensity (false colour) as a function of binding energy and in-plane wavevector for the direction $\Gamma - M$ indicated by the green dashed arrow defined in (a). The intense dispersive bands at binding energies of 2 eV and greater originate from the graphite substrate. Right: second derivatives of the same data. (d) Left: photoemission intensity as in (a) but for the in-plane wavevector in the direction $\Gamma - K$ which is close to orthogonal to the direction of (a) and which is indicated by the red dotted arrow in (a). Right: second derivatives of the same data. (e) and (f) Expanded views of the raw and second-derivative data of (a) and (b) respectively near the valence band edge.

as a function of binding energy and momentum, (a)-(c), and its second-derivative, (d)-(f), recorded using nano-ARPES for all our few-layer flakes and bulk (g)-(h) for a momentum slice in the $\Gamma - M$ direction (note, the data in (c) and (f) was not recorded over the same binding energy range as in the other panels). For this comparison, we labelled the bands of the bulk flake following the high symmetry points of the projected 2D Brillouin zone, using symbols $\bar{\Gamma}$, \bar{M} and \bar{K} to indicate that the vertical momentum component of the bands is not specified (at the photon energy used here (100 eV), ARPES probes states lying in an approximately planar surface passing near the Z point at the top of the 3D Brillouin

zone [23] shown in Fig. 2(b), i.e. $\bar{\Gamma} \approx Z$). Although the data for monolayer are not as clear as those obtained with the larger sample of Figure 2, there is a systematic trend in the band width of the uppermost valence band. Band widths were obtained from the raw experimental data by extracting photoemission counts as a function of binding energy (that is, the energy distribution curves, EDCs) and fitting these to obtain a measure of the band edge position at each momentum value, from which the energies of the extrema could be identified (for demonstration of the fits, see the SM, Fig. S4). For comparison, the band widths predicted by non-relativistic DFT calculations for the uppermost band are 95 meV (1L), 150

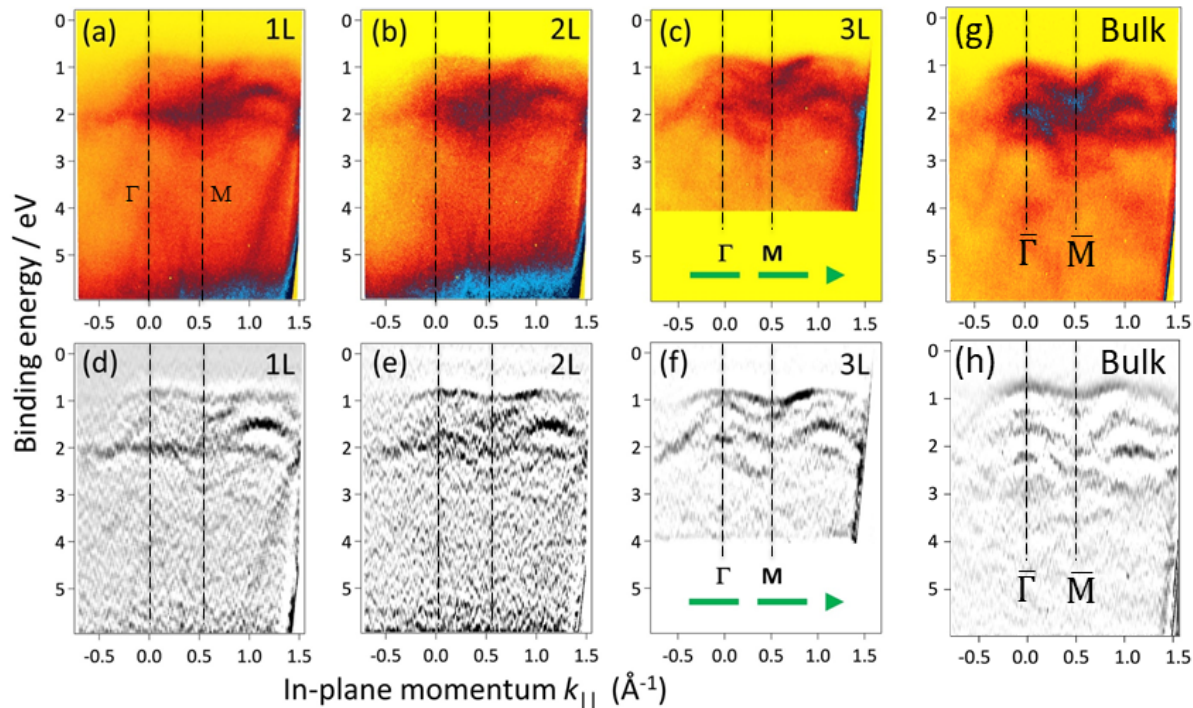


FIG. 3. Comparison of the measured ReSe_2 valence band dispersion along $\Gamma - M$ (indicated by the green dashed arrow defined in Figure 1) for mono-, bi- and tri-layer flakes (labeled 1L, 2L and 3L respectively) and bulk. (a)-(c),(g) ARPES data; (d)-(f),(h) second derivatives of the data above. Vertical dashed lines indicate the positions of the Γ and M points on each panel.

meV (2L) and 500 meV for bulk (we did not carry out a 3L calculation). For a fully relativistic calculation, we obtain similar values (85, 187 and 436 meV respectively). The calculated band structures in the $\Gamma - M$ direction are shown in the SM, Fig. S5. The trend in these band widths agrees well with the experimental measurements. The neglect of quasi-particle effects in our calculations might be expected to underestimate the band widths [44] but the calculated and experimental values are in fact very close. In Fig. 4(a), we present a comparison of the top valence bands in the $\Gamma - K$ and $\Gamma - M$ directions as extracted from the experimental data for 1L, 2L, 3L and bulk; the raw data are shown in the SM, Figs. S6-S8 (in Fig. S8 we show a comparison of the raw data with the calculated band structures of bulk and monolayer samples in the $\Gamma - K$ and $\Gamma - M$ directions). A summary of the band widths obtained from fitting the EDCs is displayed in Fig. 4(b) which illustrates the flatter VBM in the $\Gamma - M$ direction with the width along $\Gamma - K$ be-

ing comparable for three out of four investigated layer numbers. The error bars are estimated from varying the parameters of the fitting procedure and the error for the case of the bilayer in the $\Gamma - K$ direction is somewhat larger as the data is slightly poorer (see Fig. S7); the 2L region was the smallest of the flakes (see Fig. 1(a)) and therefore the most difficult to measure. Note, band width values for bulk are photon energy-dependent due to the dispersion normal to the layers; our present values agree well with previous values measured on cleaner, cleaved bulk material [23] at the same photon energy.

At the photon energy of 100 eV used here for the nano-ARPES experiments, the recorded signal is highly surface-specific: the predicted inelastic mean free path of MoS_2 , for example, ranges from 3.5 to 6.0 Å for photon energies from 70 to 170 eV respectively, [47–49] comparable to the layer thickness of ReSe_2 (c -axis 6.7 Å), and a simple estimate based on the universal curve [50] gives 5.5 Å at 100 eV. Despite this, Fig. 3 demonstrates sys-

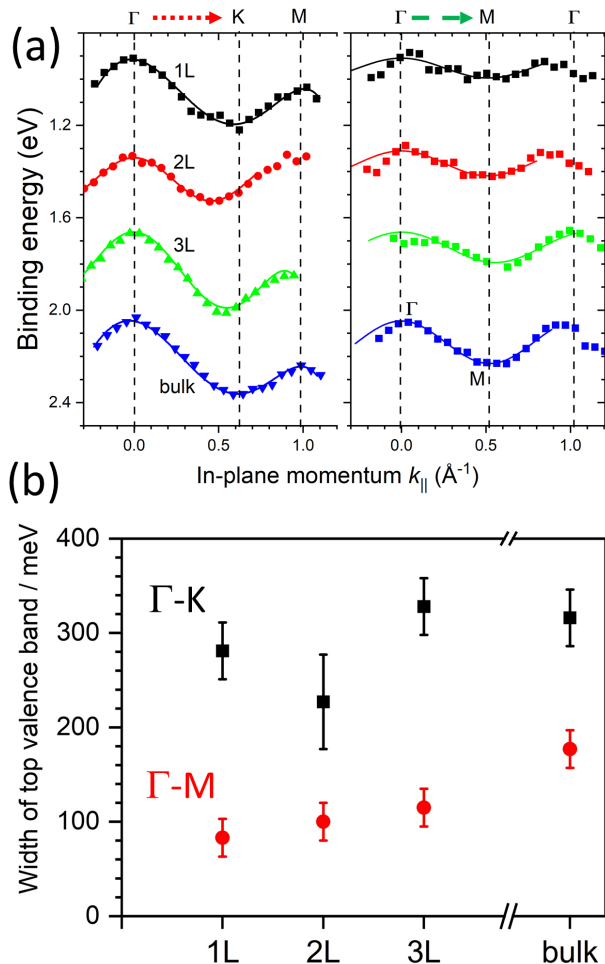


FIG. 4. Comparison of the measured ReSe_2 valence band dispersion along $\Gamma - M$ (as indicated by the green dashed arrow defined in Figure 1) for mono-, bi- and tri-layer flakes (labeled 1L, 2L and 3L respectively) and bulk; (a) band edge positions determined from an EDC fit at each wavevector, with fits to each band edge to obtain the bandwidth; (b) summary of the bandwidths obtained in $\Gamma - M$ (red circles) and $\Gamma - K$ (black squares) directions for monolayer, bilayer, trilayer and bulk ReSe_2 .

tematic changes in the valence band edge as a function of the number of layers. Overall, our nano-ARPES data reveals valence band states that are clearly dependent on inter-layer hopping interactions and must be representative of the body of the flake. We do not observe electronic states confined to individual layers except in the case of the 1L sample itself. This is in agreement with studies of bulk and few-layer ReS_2 [51, 52]. Thus, although the inter-layer interactions of ReSe_2 are weak, very similar to ReS_2 [30, 38], they are certainly non-negligible [53].

Recently, the surface-sensitivity of ARPES has been applied to reveal hidden spin polarisation [54] in centrosymmetric bulk TMDs, for example, WSe_2 [55, 56], MoS_2 [57], NbSe_2 [58], and PtSe_2 [59]. In the nomencla-

ture of spin-polarisation effects introduced by Zhang *et al.* [54], D-1 signifies a spin polarization arising from conventional bulk Dresselhaus inversion asymmetry and D-2 implies localised Dresselhaus spin polarizations compensated by their opposites under bulk inversion symmetry. The case of MoS_2 was considered theoretically [60]; $2H\text{-MoS}_2$ is a system where individual D-1 layers interact (weakly) to give D-2 behaviour in bulk. Surface-sensitive techniques such as STM or ARPES can probe the top layer of a bulk crystal and can reveal its D-1 nature. However, once again, ReX_2 proves to be an untypical member of the TMD family, because its structure contains a centre of inversion at the midpoint of each diamond of four Re atoms. On symmetry grounds, therefore, even a monolayer is only expected to show D-2 behaviour. The opposing spin polarisations reside on Re atoms located close to one another in the same layer, meaning that the near single-layer sensitivity of ARPES cannot resolve individual D-1 contributions. This is borne out by the lack of observed spin-orbit splittings here or in any earlier ARPES data on bulk or few-layer ReX_2 [20, 23, 44, 51, 52, 61].

D. Comparison of bulk and monolayer ReSe_2

Making use of our variety of flake thicknesses, we also study in more detail the differences between the monolayer and bulk dispersions. Although studies of the ARPES of bulk ReSe_2 were already reported [23, 44, 62], we benefit from the fact that the present exfoliated samples have identical crystallographic orientations. Furthermore, the ability to detect the graphite band structure removes any ambiguity about the location of the first Brillouin zone of the bulk material. This is useful because in the bulk, the crystallographic c axis is not perpendicular to the plane so that the surface in reciprocal space probed by ARPES for a set photon energy intersects successive Brillouin zones at different heights and so the measured bulk band structure is not periodic in the in-plane momentum [23, 51, 52, 61, 62].

We investigated the orbital character of the valence band of monolayer and bulk ReSe_2 using density functional theory calculations and show the key results for monolayer in Fig. 5 (projections for the bulk are shown in SM). In these calculations, we have neglected the spin-orbit coupling so that the atomic wavefunctions are purely orbital angular momentum states (this is acceptable because inversion symmetry which forbids any band spin splitting is present for all crystal thicknesses, even monolayer). For this discussion, x, y are defined as the directions along and normal to the Re chains respectively and z is normal to the layer, as in panel (a). We also focus on orbital projections of representative atomic sites while a more complete set is given in the SM.

We note that the four selenium sites that are not related by symmetry make different contributions to the band structure and, of these, one can identify two main

types of chalcogen site; those located on the Re diamonds, labeled atoms 3 and 4 in Fig. 5(a), and those bridging adjacent Re chains (atoms 5 and 6) which differ markedly. Evidence for the non-equivalence of these sites is also provided by Raman spectroscopy studies of $\text{ReSe}_{2-x}\text{S}_x$ alloys which showed that the substitution of sulphur on the different chalcogen sites yields different formation energies and vibrational frequencies [23] whilst high resolution electron microscopy suggests preferential occupation of the more stable sites by impurities [63]. Scanning tunneling microscopy (STM) and spectroscopy (STS) likewise show very clearly the non-equivalence of the four selenium sites in ReSe_2 [64].

Considering the projections of the valence band states onto the Se p orbitals, shown in Fig. 5, panels (b) to (g), it is clear that it is the Se p_x orbitals of Se sites 4 (and 3, see Figure S11) that contribute to the flat VBM in the $\Gamma - M$ direction (marked by the blue arrow on panel (e)). As seen in panel (b), there is a similar but smaller Se p_x contribution to the valence band edge from site 5. From the coordinate system shown in Fig. 5(a), it is clear that the p_x states of sites 3 and 4 are polarized along the Re chains and are spatially localized on top of them. The interaction between the orbitals of Se sites 3 and 4 on neighboring chains is minimal, and there is a near-absence of dispersion in the $\Gamma - M$ (y) direction. On the other hand, there is a significant dispersion along $\Gamma - K$ (x) direction, which can be seen in Fig. 4. As seen in panels (c,d) and (f,g), this intrachain dispersion is not due to Se p -orbitals. Instead, as shown in the SM, it is generated predominantly by Re d -orbitals (with main contributions from $d_{x^2-y^2}$ and d_{zy}). Finally, we note that the contributions of all Se p_z orbitals to the valence band edge are very small (see Figs. S10 and S11).

IV. SUMMARY

We have demonstrated that in ReSe_2 in-plane anisotropy is quite uniquely coupled to interlayer interaction so that decreasing the number of layers in the crystal decreases the dispersion in direction perpendicular to the rhenium chains ($\Gamma - M$ in reciprocal space). This implies increasing interchain decoupling and a growing one-dimensional character of electronic states in this material. The extremely flat valence band dispersion perpendicular to the Re chains implies that, in monolayer ReSe_2 , hole transport should be dominated by conduction along the direction of the Re chains and thus should be extremely anisotropic. No experimental test of this has yet been carried out, though it is established that the in-plane mobility is lowest perpendicular to the Re chains in bulk-like material. An anisotropy of about a factor of two between mobilities in the a and b directions was reported for few-layer $\text{ReSe}_{2-x}\text{S}_x$ devices [65] but their reported number of layers was ~ 5 which, as shown above, is too thick to observe the present effects; furthermore, they observed n -type conductivity. Another study

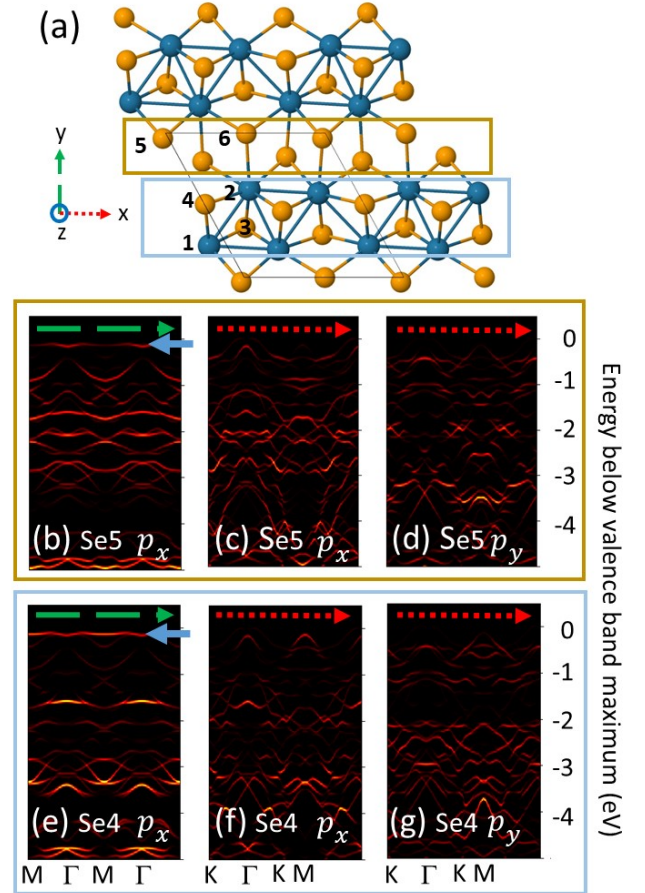


FIG. 5. The valence band structure of monolayer ReSe_2 analysed in terms of the atomic orbitals of selenium. (a) top view of ReSe_2 showing the numbering of the atoms: 1,2 are Re, 3-6 are Se. Other atoms are related to these by symmetry. Rectangular boxes show the assignment of the chalcogen atoms to two families, those between rhenium chains (upper yellow box) and those above and below the chains (lower blue box). (b)-(g) Calculated valence band states projected onto the selected Se atomic orbitals identified on each panel for the in-plane momentum directions $\Gamma - M$ and $\Gamma - K$ defined in Fig. 2 (reciprocal space directions are indicated by dashed green arrows and dotted red arrows respectively at the top of each panel). The top of the valence band is defined as the zero of energy and the blue arrows in panels (b) and (e) mark the near-dispersionless state discussed in the text.

found an anisotropy ratio of ~ 4 for n -type conductivity in W-doped bulk material [66] in agreement with a recent ARPES study [62]. Several other studies on exfoliated material likewise used few-layer flakes down to 3L, or n -type material, and so do not provide a test of the present predictions [67–71]. There is only one report of measurements on p -type conductivity in a monolayer, where a hole mobility of $10 \text{ cm}^2\text{V}^{-1}\text{s}^{-1}$ was found, but the anisotropy of the charge transport was apparently not investigated [71]. It is therefore a high priority to investigate transport in monolayer ReSe_2 in suitably de-

signed structures which would ideally allow for investigation both of the predicted anisotropy but also electrostatic gating to ensure hole transport dominates. The quasi-one dimensional nature of hole transport in ReSe₂ offers the possibility of a momentum-selective filter or contact to other TMD layers in either lateral or vertical heterostructures.

ACKNOWLEDGMENTS

This work was supported by the Centre for Graphene Science of the Universities of Bath and Exeter and by the EPSRC (UK) under grants EP/G036101, EP/M022188,

and EP/P004830; L.S.H. and S.G. are supported by the Bath/Bristol Centre for Doctoral Training in Condensed Matter Physics, EPSRC grant EP/L015544. M.M-K. acknowledges support from the University of Bath International Funding Scheme. We thank the SOLEIL synchrotron for the provision of beam time; work at SOLEIL was supported by EPSRC grant EP/P004830/1. The present collaborative research was undertaken in the context of the Associated Unit MATINÉE of the Spanish Scientific Research Council (CSIC). Computational work was performed on the University of Bath's High Performance Computing Facility. Data created during this research are freely available from the University of Bath data archive at DOI:10.15125/BATH-00521.

-
- [1] M. Bahramy, O. Clark, B.-J. Yang, J. Feng, L. Bawden, J. Riley, I. Marković, F. Mazzola, V. Sunko, and D. Biswas, Ubiquitous formation of bulk Dirac cones and topological surface states from a single orbital manifold in transition-metal dichalcogenides, *Nature Materials* **17**, 21 (2018).
- [2] K. F. Mak and J. Shan, Photonics and optoelectronics of 2D semiconductor transition metal dichalcogenides, *Nature Photonics* **10**, 216 (2016).
- [3] Q. H. Wang, K. Kalantar-Zadeh, A. Kis, J. N. Coleman, and M. S. Strano, Electronics and optoelectronics of two-dimensional transition metal dichalcogenides, *Nature Nanotechnology* **7**, 699 (2012).
- [4] P. K. Nayak, Y. Horbatenko, S. Ahn, G. Kim, J.-U. Lee, K. Y. Ma, A. R. Jang, H. Lim, D. Kim, S. Ryu, H. Cheong, N. Park, and H. S. Shin, Probing evolution of twist-angle-dependent interlayer excitons in MoSe₂/WSe₂ van der Waals heterostructures, *ACS Nano* **11**, 4041 (2017).
- [5] Y. He, Y. Yang, Z. Zhang, Y. Gong, W. Zhou, Z. Hu, G. Ye, X. Zhang, E. Bianco, S. Lei, Z. Jin, X. Zou, Y. Yang, Y. Zhang, E. Xie, J. Lou, B. Yakobson, R. Vajtai, B. Li, and P. Ajayan, Strain-induced electronic structure changes in stacked van der Waals heterostructures, *Nano Letters* **16**, 3314 (2016).
- [6] Y. Li, K.-A. N. Duerloo, K. Wauson, and E. J. Reed, Structural semiconductor-to-semimetal phase transition in two-dimensional materials induced by electrostatic gating, *Nature Communications* **7**, 10671 (2016).
- [7] H.-J. Lamfers, A. Meetsma, G. Wiegers, and J. de Boer, The crystal structure of some rhenium and technetium dichalcogenides, *Journal of Alloys and Compounds* **241**, 34 (1996).
- [8] M. Rahman, K. Davey, and S.-Z. Qiao, Advent of 2D rhenium disulfide (ReS₂): Fundamentals to applications, *Advanced Functional Materials* **27**, 1606129 (2017).
- [9] L. Wang, Z. Sofer, J. Luxa, D. Sedmidubský, A. Ambrosi, and M. Pumera, Layered rhenium sulfide on free-standing three-dimensional electrodes is highly catalytic for the hydrogen evolution reaction: Experimental and theoretical study, *Electrochemistry Communications* **63**, 39 (2016).
- [10] J. A. Aliaga, T. Zepeda, J. F. Araya, F. Paraguay-Delgado, E. Benavente, G. Alonso-Núñez, S. Fuentes, and G. González, Low-dimensional ReS₂/C composite as effective hydrodesulfurization catalyst, *Catalysts* **7**, 377 (2017).
- [11] H. Zhao, Z. Dai, X. Xu, J. Pan, and J. Hu, Integrating semiconducting catalyst of ReS₂ nanosheets into p-silicon photocathode for enhanced solar water reduction, *ACS Applied Materials & Interfaces* **10**, 23074 (2018).
- [12] A. Splendiani, L. Sun, Y. Zhang, T. Li, J. Kim, C.-Y. Chim, G. Galli, and F. Wang, Emerging photoluminescence in monolayer MoS₂, *Nano Letters* **10**, 1271 (2010).
- [13] W. Jin, P.-C. Yeh, N. Zaki, D. Zhang, J. T. Sadowski, A. Al-Mahboob, A. M. van Der Zande, D. A. Chenet, J. I. Dadap, I. P. Herman, P. Sutter, J. Hone, and R. M. Osgood Jr., Direct measurement of the thickness-dependent electronic band structure of MoS₂ using angle-resolved photoemission spectroscopy, *Physical Review Letters* **111**, 106801 (2013).
- [14] Y. Zhang, T.-R. Chang, B. Zhou, Y.-T. Cui, H. Yan, Z. Liu, F. Schmitt, J. Lee, R. Moore, Y. Chen, H. Lin, H.-T. Jeng, S.-K. Mo, Z. Hussain, A. Bansil, and Z.-X. Shen, Direct observation of the transition from indirect to direct bandgap in atomically thin epitaxial MoSe₂, *Nature Nanotechnology* **9**, 111 (2014).
- [15] C. S. Jung, F. Shojaei, K. Park, J. Y. Oh, H. S. Im, D. M. Jang, J. Park, and H. S. Kang, Red-to-ultraviolet emission tuning of two-dimensional gallium sulfide/selenide, *ACS Nano* **9**, 9585 (2015).
- [16] Z. Ben Aziza, D. Pierucci, H. Henck, M. G. Silly, C. David, M. Yoon, F. Sirotti, K. Xiao, M. Eddrief, J.-C. Girard, and A. Ouerghi, Tunable quasiparticle band gap in few-layer GaSe/graphene van der Waals heterostructures, *Physical Review B* **96**, 035407 (2017).
- [17] M. J. Hamer, J. Zultak, A. V. Tyurnina, V. Zólyomi, D. Terry, A. Barinov, A. Garner, J. Donoghue, A. P. Rooney, V. Kandyba, A. Giampietri, A. Graham, N. Teutsch, X. Xia, M. Koperski, S. J. Haigh, V. I. Fal'ko, R. V. Gorbachev, and N. R. Wilson, Indirect to direct gap crossover in two-dimensional InSe revealed by angle-resolved photoemission spectroscopy, *ACS Nano* **13**, 2136 (2019).
- [18] H. Yuan, X. Liu, F. Afshinmanesh, W. Li, G. Xu, J. Sun, B. Lian, A. G. Curto, G. Ye, Y. Hikita, Z. Shen, S.-C. Zhang, X. Chen, M. Brongersma, H. Y. Hwang, and Y. Cui, Polarization-sensitive broadband photodetector

- using a black phosphorus vertical p-n junction, *Nature Nanotechnology* **10**, 707 (2015).
- [19] M. Kertesz and R. Hoffmann, Octahedral vs trigonal-prismatic coordination and clustering in transition-metal dichalcogenides, *Journal of the American Chemical Society* **106**, 3453 (1984).
- [20] B. K. Choi, S. Ulstrup, S. M. Gunasekera, J. Kim, S. Y. Lim, L. Moreschini, J. S. Oh, S.-H. Chun, C. Jozwiak, A. Bostwick, E. Rotenberg, H. Cheong, I.-W. Lyo, M. Mucha-Kruczynski, and Y. J. Chang, Visualizing orbital content of electronic bands in anisotropic 2D semiconducting ReSe₂, *ACS Nano* **14**, 7880 (2020).
- [21] See Supplemental Material at URL for optical and AFM images of monolayer and few-layer flakes; photoemission energy distribution curves for monolayer ReSe₂; calculated VB dispersion in the $\Gamma - M$ direction for few-layer and bulk ReSe₂; measured VB dispersions of few-layer ReSe₂ and their second derivatives; comparison of calculated and experimental dispersions of ReSe₂; projections of calculated VB dispersion onto Se *p*- and Re *d*-orbitals in $\Gamma - K$ and $\Gamma - M$ directions.
- [22] J. J. Yeh and I. Lindau, Atomic subshell photoionization cross sections and asymmetry parameters: $1 \leq z \leq 103$, *Atomic Data and Nuclear Data Tables* **32**, 1 (1985).
- [23] L. S. Hart, J. L. Webb, S. Dale, S. J. Bending, M. Mucha-Kruczynski, D. Wolverson, C. Chen, J. Avila, and M. C. Asensio, Electronic bandstructure and van der waals coupling of ReSe₂ revealed by high-resolution angle-resolved photoemission spectroscopy, *Scientific Reports* **7**, 5145 (2017).
- [24] P. Giannozzi, S. Baroni, N. Bonini, M. Calandra, R. Car, C. Cavazzoni, D. Ceresoli, G. L. Chiarotti, M. Cococcioni, I. Dabo, A. Dal Corso, S. de Gironcoli, S. Fabris, G. Fratesi, R. Gebauer, U. Gerstmann, C. Gougoussis, A. Kokalj, M. Lazzeri, L. Martin-Samos, N. Marzari, F. Mauri, R. Mazzarello, S. Paolini, A. Pasquarello, L. Paulatto, C. Sbraccia, S. Scandolo, G. Sclauzero, A. P. Seitsonen, A. Smogunov, P. Umari, and R. M. Wentzcovitch, QUANTUM ESPRESSO: a modular and open-source software project for quantum simulations of materials, *Journal of Physics: Condensed Matter* **21**, 395502 (2009).
- [25] P. E. Blöchl, Projector augmented-wave method, *Physical Review B* **50**, 17953 (1994).
- [26] G. Kresse and D. Joubert, From ultrasoft pseudopotentials to the projector augmented-wave method, *Physical Review B* **59**, 1758 (1999).
- [27] H. J. Monkhorst and J. D. Pack, Special points for brillouin-zone integrations, *Physical Review B* **13**, 5188 (1976).
- [28] D. Wolverson, S. Crampin, A. S. Kazemi, A. Ilie, and S. J. Bending, Raman spectra of monolayer, few-layer, and bulk ReSe₂: An anisotropic layered semiconductor, *ACS Nano* **8**, 11154 (2014).
- [29] S. M. Gunasekera, D. Wolverson, L. S. Hart, and M. Mucha-Kruczynski, Electronic band structure of rhenium dichalcogenides, *Journal of Electronic Materials* **47**, 4314 (2018).
- [30] H. Zhao, J. Wu, H. Zhong, Q. Guo, X. Wang, F. Xia, L. Yang, P. Tan, and H. Wang, Interlayer interactions in anisotropic atomically thin rhenium diselenide, *Nano Research* **8**, 3651 (2015).
- [31] H.-X. Zhong, S. Gao, J.-J. Shi, and L. Yang, Quasiparticle band gaps, excitonic effects, and anisotropic optical properties of the monolayer distorted 1T' diamond-chain structures ReS₂ and ReSe₂, *Physical Review B* **92**, 115438 (2015).
- [32] L. Hart, S. Dale, S. Hoye, J. L. Webb, and D. Wolverson, Rhenium dichalcogenides: layered semiconductors with two vertical orientations, *Nano Letters* **16**, 1381 (2016).
- [33] A. McCreary, J. R. Simpson, Y. Wang, D. Rhodes, K. Fujisawa, L. Balicas, M. Dubey, V. H. Crespi, M. Terrones, and A. R. Hight Walker, Intricate resonant raman response in anisotropic res₂, *Nano Letters* **17**, 5897 (2017).
- [34] E. Liu, Y. Fu, Y. Wang, Y. Feng, H. Liu, X. Wan, W. Zhou, B. Wang, L. Shao, C.-H. Ho, Y.-S. Huang, Z. Cao, L. Wang, A. Li, J. Zeng, F. Song, X. Wang, Y. Shi, H. Yuan, H. Y. Hwang, Y. Cui, F. Miao, and D. Xing, Integrated digital inverters based on two-dimensional anisotropic ReS₂ field-effect transistors, *Nature Communications* **6**, 6991 (2015).
- [35] D. A. Chenet, O. B. Aslan, P. Y. Huang, C. Fan, A. M. van der Zande, T. F. Heinz, and J. C. Hone, In-plane anisotropy in mono- and few-layer ReS₂ probed by raman spectroscopy and scanning transmission electron microscopy, *Nano Letters* **15**, 5667 (2015).
- [36] B. Jariwala, A. Thamizhavel, and A. Bhattacharya, ReSe₂: a reassessment of crystal structure and thermal analysis, *Journal of Physics D: Applied Physics* **50**, 044001 (2016).
- [37] P. Blake, E. Hill, A. Castro Neto, K. Novoselov, D. Jiang, R. Yang, T. Booth, and A. Geim, Making graphene visible, *Applied Physics Letters* **91**, 063124 (2007).
- [38] S. Tongay, H. Sahin, C. Ko, A. Luce, W. Fan, K. Liu, J. Zhou, Y.-S. Huang, C.-H. Ho, J. Yan, D. F. Ogletree, S. Aloni, J. Ji, S. Li, J. Li, F. M. Peeters, and J. Wu, Monolayer behaviour in bulk ReS₂ due to electronic and vibrational decoupling, *Nature Communications* **5**, 3252 (2014).
- [39] W. Smekal, W. S. M. Werner, and C. J. Powell, Simulation of electron spectra for surface analysis (SESSA): a novel software tool for quantitative Auger-electron spectroscopy and X-ray photoelectron spectroscopy, *Surface and Interface Analysis* **37**, 1059 (2005).
- [40] C. Ho, Y. Huang, J. Chen, T. Dann, and K. Tiong, Electronic structure of ReS₂ and ReSe₂ from first-principles calculations, photoelectron spectroscopy, and electrolyte electroreflectance, *Physical Review B* **60**, 15766 (1999).
- [41] C. H. Ho, Y. S. Huang, K. K. Tiong, and P. C. Liao, Absorption-edge anisotropy in ReS₂ and ReSe₂ layered semiconductors, *Physical Review B* **58**, 16130 (1998).
- [42] C.-H. Ho, H. Lee, and C. Wu, Polarization sensitive behaviour of the band-edge transitions in ReS₂ and ReSe₂ layered semiconductors, *Journal of Physics: Condensed Matter* **16**, 5937 (2004).
- [43] C. Ho, M. Hsieh, C. Wu, Y. Huang, and K. Tiong, Dichroic optical and electrical properties of rhenium dichalcogenides layer compounds, *Journal of Alloys and Compounds* **442**, 245 (2007).
- [44] P. Eickholt, J. Noky, E. Schwier, K. Shimada, K. Miyamoto, T. Okuda, C. Datzler, M. Drüppel, P. Krüger, M. Rohlffing, and M. Donath, Location of the valence band maximum in the band structure of anisotropic 1T'-ReSe₂, *Physical Review B* **97**, 165130 (2018).
- [45] N. R. Wilson, P. V. Nguyen, K. Seyler, P. Rivera, A. J. Marsden, Z. P. L. Laker, G. C. Constantinescu, V. Kandyba, A. Barinov, N. D. M. Hine, X. Xu, and

- D. H. Cobden, Determination of band offsets, hybridization, and exciton binding in 2D semiconductor heterostructures, *Science Advances* **3**, e1601832 (2017).
- [46] H. Coy Diaz, J. Avila, C. Chen, R. Addou, M. C. Asensio, and M. Batzill, Direct observation of interlayer hybridization and Dirac relativistic carriers in graphene/MoS₂ van der Waals heterostructures, *Nano Letters* **15**, 1135 (2015).
- [47] S. W. Han, G.-B. Cha, E. Frantzeskakis, I. Razado-Colambo, J. Avila, Y. S. Park, D. Kim, J. Hwang, J. S. Kang, S. Ryu, W. S. Yun, S. C. Hong, and M. C. Asensio, Band-gap expansion in the surface-localized electronic structure of MoS₂(0002), *Physical Review B* **86**, 115105 (2012).
- [48] J. R. Lince, T. B. Stewart, M. M. Hills, P. D. Fleischauer, J. A. Yarmoff, and A. Taleb-Ibrahimi, Chemical effects of Ne⁺ bombardment on the MoS₂(0001) surface studied by high-resolution photoelectron spectroscopy, *Surface Science* **210**, 387 (1989).
- [49] S. Tanuma, C. J. Powell, and D. R. Penn, Proposed formula for electron inelastic mean free paths based on calculations for 31 materials, *Surface Science* **192**, L849 (1987).
- [50] M. P. Seah and W. A. Dench, Quantitative electron spectroscopy of surfaces: A standard data base for electron inelastic mean free paths in solids, *Surface and Interface Analysis* **1**, 2 (1979).
- [51] D. Biswas, A. M. Ganose, R. Yano, J. Riley, L. Bawden, O. Clark, J. Feng, L. Collins-McIntyre, M. Sajjad, W. Meevasana, T. K. Kim, M. Hoesch, J. E. Rault, T. Sasagawa, D. O. Scanlon, and P. D. C. King, Narrow-band anisotropic electronic structure of ReS₂, *Physical Review B* **96**, 085205 (2017).
- [52] M. Gehlmann, I. Aguilera, G. Bihlmayer, S. Nemsák, P. Nagler, P. Gospodarič, G. Zamborlini, M. Eschbach, V. Feyer, F. Kronast, E. Młyńczak, T. Korn, L. Plucinski, C. Schüller, S. Blügel, and C. M. Schneider, Direct observation of the band gap transition in atomically thin ReS₂, *Nano Letters* **17**, 5187 (2017).
- [53] J. Echeverry and I. Gerber, Theoretical investigations of the anisotropic optical properties of distorted 1T-ReS₂ and ReSe₂ monolayers, bilayers, and in the bulk limit, *Physical Review B* **97**, 075123 (2018).
- [54] X. Zhang, Q. Liu, J.-W. Luo, A. J. Freeman, and A. Zunger, Hidden spin polarization in inversion-symmetric bulk crystals, *Nature Physics* **10**, 387 (2014).
- [55] J. M. Riley, F. Mazzola, M. Dendzik, M. Michiardi, T. Takayama, L. Bawden, C. Granerød, M. Leandersson, T. Balasubramanian, M. Hoesch, T. K. Kim, H. Takagi, W. Meevasana, P. Hofmann, M. S. Bahramy, J. W. Wells, and P. D. C. King, Direct observation of spin-polarized bulk bands in an inversion-symmetric semiconductor, *Nature Physics* **10**, 835 (2014).
- [56] R. Bertoni, C. W. Nicholson, L. Waldecker, H. Hübener, C. Monney, U. De Giovannini, M. Puppini, M. Hoesch, E. Springate, and R. T. Chapman, Generation and evolution of spin-, valley-, and layer-polarized excited carriers in inversion-symmetric WSe₂, *Physical Review Letters* **117**, 277201 (2016).
- [57] M. Gehlmann, I. Aguilera, G. Bihlmayer, E. Młyńczak, M. Eschbach, S. Döring, P. Gospodarič, S. Cramm, B. Kardynał, L. Plucinski, S. Blügel, and C. M. Schneider, Quasi 2D electronic states with high spin-polarization in centrosymmetric MoS₂ bulk crystals, *Scientific Reports* **6**, 26197 (2016).
- [58] L. Bawden, S. Cooil, F. Mazzola, J. Riley, L. Collins-McIntyre, V. Sunko, K. Hunvik, M. Leandersson, C. Polley, and T. Balasubramanian, Spin-valley locking in the normal state of a transition-metal dichalcogenide superconductor, *Nature Communications* **7**, 11711 (2016).
- [59] W. Yao, E. Wang, H. Huang, K. Deng, M. Yan, K. Zhang, K. Miyamoto, T. Okuda, L. Li, Y. Wang, H. Gao, C. Liu, W. Duan, and S. Zhou, Direct observation of spin-layer locking by local Rashba effect in monolayer semiconducting PtSe₂ film, *Nature Communications* **8**, 14216 (2017).
- [60] Q. Liu, X. Zhang, H. Jin, K. Lam, J. Im, A. J. Freeman, and A. Zunger, Search and design of nonmagnetic centrosymmetric layered crystals with large local spin polarization, *Physical Review B* **91**, 235204 (2015).
- [61] J. L. Webb, L. S. Hart, D. Wolverson, C. Chen, J. Avila, and M. C. Asensio, Electronic band structure of ReS₂ by high-resolution angle-resolved photoemission spectroscopy, *Physical Review B* **96**, 115205 (2017).
- [62] B. S. Kim, W. S. Kyung, J. D. Denlinger, C. Kim, and S. R. Park, Strong one-dimensional characteristics of hole-carriers in ReS₂ and ReSe₂, *Scientific Reports* **9**, 2730 (2019).
- [63] W. Wen, J. Lin, K. Suenaga, Y. Guo, Y. Zhu, H.-P. Hsu, and L. Xie, Preferential S/Se occupation in an anisotropic ReS_{2-x}Se_{2x} monolayer alloy, *Nanoscale* **9**, 18275 (2017).
- [64] M. Hong, X. Zhou, N. Gao, S. Jiang, C. Xie, L. Zhao, Y. Gao, Z. Zhang, P. Yang, Y. Shi, Q. Zhang, Z. Liu, J. Zhao, and Y. Zhang, Identifying the non-identical outermost selenium atoms and invariable band gaps across the grain boundary of anisotropic rhenium diselenide, *ACS Nano* **12**, 10095 (2018).
- [65] F. C. Liu, S. J. Zheng, A. Chaturvedi, V. Zolyomi, J. D. Zhou, Q. D. Fu, C. Zhu, P. Yu, Q. S. Zeng, N. D. Drummond, H. J. Fan, C. Kloc, V. I. Fal'ko, X. X. He, and Z. Liu, Optoelectronic properties of atomically thin ReSSe with weak interlayer coupling, *Nanoscale* **8**, 5826 (2016).
- [66] S. Hu, C. Liang, K. Tiong, Y. Huang, and Y. Lee, Electrical anisotropy of W-doped ReSe₂ crystals, *Journal of The Electrochemical Society* **153**, J1100 (2006).
- [67] C. M. Corbet, C. McClellan, A. Rai, S. S. Sonde, E. Tutuc, and S. K. Banerjee, Field effect transistors with current saturation and voltage gain in ultrathin ReS₂, *ACS Nano* **9**, 363 (2015).
- [68] M. H. Ali, D.-H. Kang, and J.-H. Park, Rhenium diselenide (ReSe₂) infrared photodetector enhanced by (3-aminopropyl) trimethoxysilane (APTMS) treatment, *Organic Electronics* **53**, 14 (2018).
- [69] E. Zhang, P. Wang, Z. Li, H. Wang, C. Song, C. Huang, Z.-G. Chen, L. Yang, K. Zhang, S. Lu, W. Wang, S. Liu, H. Fang, X. Zhou, H. Yan, J. Zou, X. Wan, P. Zhou, W. Hu, and F. Xiu, Tunable ambipolar polarization-sensitive photodetectors based on high-anisotropy ReSe₂ nanosheets, *ACS Nano* **10**, 8067 (2016).
- [70] S. Yang, S. Tongay, Q. Yue, Y. Li, B. Li, and F. Lu, High-performance few-layer Mo-doped ReSe₂ nanosheet photodetectors, *Scientific Reports* **4**, 5442 (2014).
- [71] S. Yang, S. Tongay, Y. Li, Q. Yue, J.-B. Xia, S.-S. Li, J. Li, and S.-H. Wei, Layer-dependent electrical and optoelectronic responses of ReSe₂ nanosheet transistors, *Nanoscale* **6**, 7226 (2014).

Supplemental Material:

Interplay of crystal thickness and in-plane anisotropy and evolution of quasi-one dimensional electronic character in ReSe₂

Lewis S. Hart,¹ Surani M. Gunasekera,¹ James L. Webb,¹ Marcin Mucha-Kruczyński,¹ José Avila,² María C. Asensio,³ and Daniel Wolverson¹

¹*Centre for Nanoscience and Nanotechnology and Department of Physics, University of Bath, Bath BA2 7AY, United Kingdom*

²*Synchrotron SOLEIL, Saint Aubin and Université Paris-Saclay, BP 48 91192 Gif-sur-Yvette, France*

³*Madrid Institute of Materials Science (ICMM), Spanish Scientific Research Council (CSIC), Cantoblanco, E-28049 Madrid, Spain*

CONTENTS

S1. List of figures	2
S2. Sample preparation.	3
S3. Sample characterization.	3
References	20

S1. LIST OF FIGURES

- Figure S1: optical and AFM images of monolayer flakes
- Figure S2: optical and AFM data for few-layer flakes
- Figure S3: photoemission energy distribution curves for monolayer ReSe₂
- Figure S4: PES energy distribution curves for 1L, 2L, 3L and bulk ReSe₂
- Figure S5: calculated VB dispersion in the $\Gamma - M$ direction for few-layer and bulk ReSe₂
- Figure S6 comparison of 1L and bulk ReSe₂ ARPES in $\Gamma - M$ and $\Gamma - K$ directions
- Figure S7: measured VB dispersions of few-layer ReSe₂
- Figure S8: second derivatives of VB dispersions of few-layer ReSe₂
- Figure S9: comparison of calculated and experimental dispersions of ReSe₂
- Figure S10: projection of calculated VB dispersion onto Se p -orbitals ($\Gamma - K$)
- Figure S11: projection of calculated VB dispersion onto Se p -orbitals ($\Gamma - M$)
- Figure S12: projection of calculated VB dispersion onto Re d -orbitals ($\Gamma - K$)
- Figure S13: projection of calculated VB dispersion onto Re d -orbitals ($\Gamma - M$)
- Figure S14: projection of calculated VB dispersion onto Se p -orbitals ($\Gamma - Z$)
- Figure S15: projection of calculated VB dispersion onto Re d -orbitals ($\Gamma - Z$)

S2. SAMPLE PREPARATION.

ReSe₂ samples were prepared in air by micro-mechanical cleavage (exfoliation) from bulk single crystals grown by chemical vapour transport and supplied by HQ Graphene. The cleaved flakes were transferred to a PDMS film for solvent-free transfer to a large highly oriented pyrolytic graphite (HOPG) flake on a conducting silicon substrate [1]. The HOPG platform (with dimensions of several 100 μm) provides a conducting link to the grounded silicon substrate to prevent the ReSe₂ layers charging during measurement (essential for both imaging and spectroscopy) and assists in locating the ReSe₂ layers in the ARPES experiment. Samples were washed with acetone and isopropanol to remove organic residues and were then annealed in argon for 5 hours at 400 °C; annealing results in coalescence of material trapped under the layer into relatively few, large bubbles with flat regions in between, as revealed by atomic force microscopy (AFM) and as observed also for WSe₂ [2] (in contrast to Ref. [2], however, no graphene capping layer was used). Once mounted in the beamline, samples were annealed again in UHV at 400 °C for over 12 hours.

S3. SAMPLE CHARACTERIZATION.

Atomic force microscopy (AFM) line scans across step edges were used to confirm the ReSe₂ layer thicknesses and AFM imaging was used to assess the flatness of the layers; optical microscopy and AFM images are shown in Figure S1 of the Supporting Information. Layer composition and thicknesses were checked via Raman microscopy as shown in Figure 1; a Renishaw InVia system was used with 532 nm excitation and a $\times 100$ objective, giving a spatial resolution of better than 1 μm , adequate to select each of the 1L, 2L and 3L regions in turn. Since the ReSe₂ layers were placed on thick HOPG platforms and the substrate did not have a thermal SiO₂ layer, interference effects did not modify the intensity of the Raman spectra, which was found to depend linearly on the number of layers as discussed earlier. Finally, Re core level X-ray photoemission spectra (XPS), integrated over the binding energy range 40-44 eV, were used to image the ReSe₂ layers; individual XPS spectra also confirmed the bonding of Re to Se.

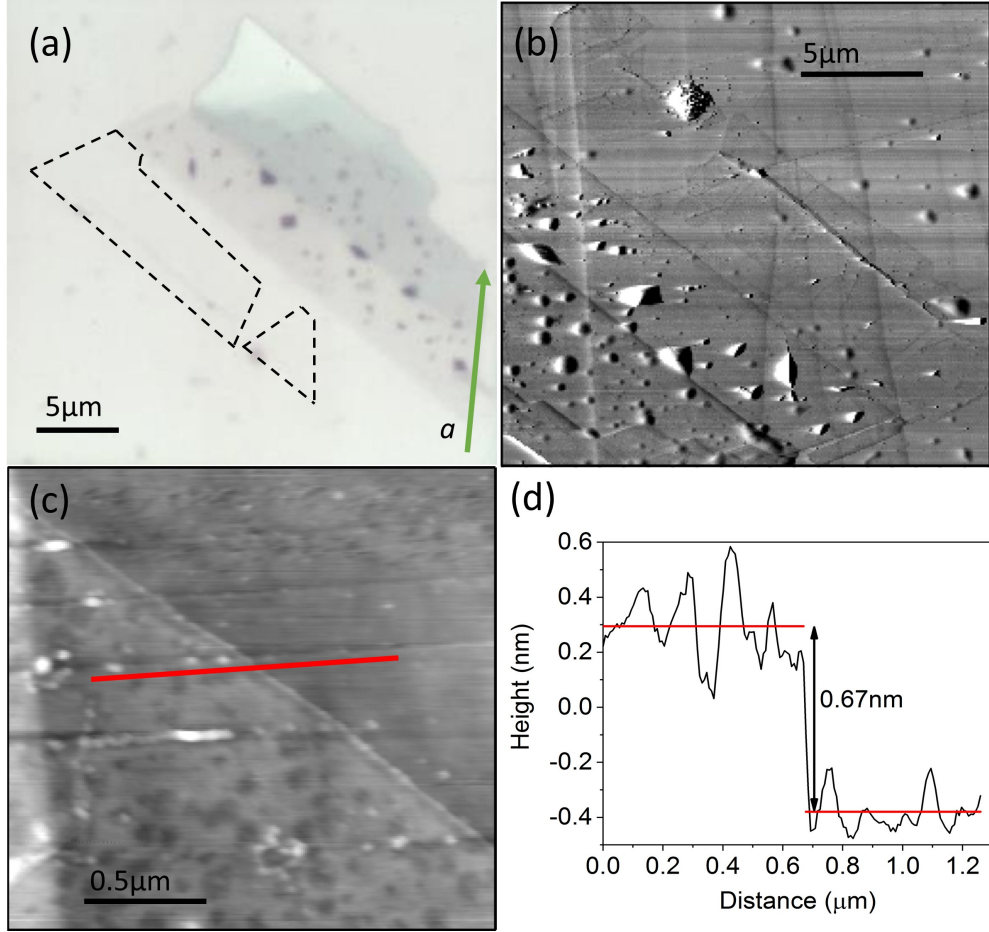


FIG. S1. (a) Optical image of the ReSe_2 monolayer after placing on the HOPG support and annealing. The dashes show the outlines of two monolayer regions, of which the larger was used in the ARPES work; (b) an AFM phase image of that monolayer, showing bubbles of material trapped under the layer developed during annealing; (c) an AFM image of the edge of the flake showing (red solid line) the path used to make the thickness measurement in (d).

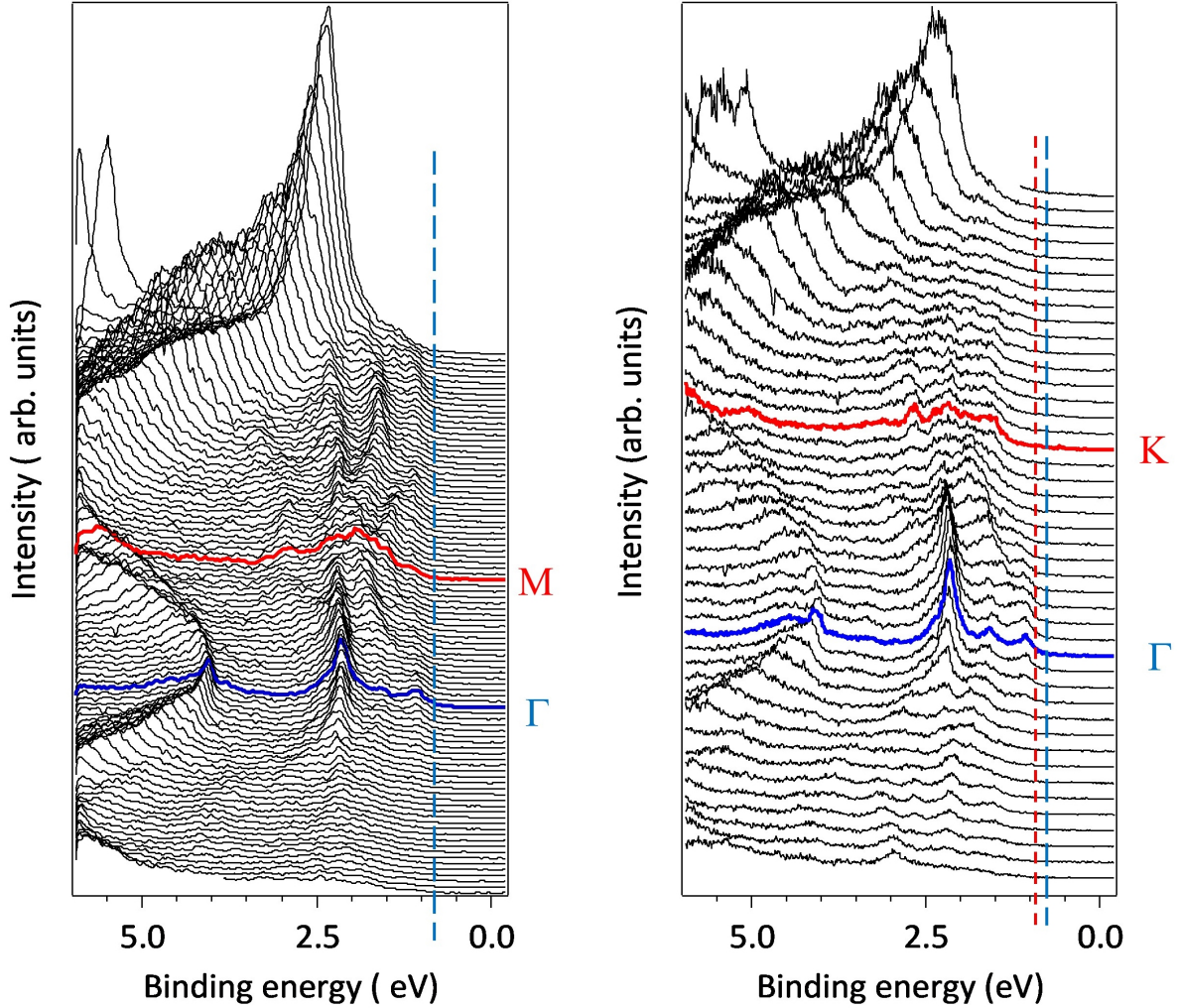


FIG. S2. (a) Optical image of the 1L, 2L and 3L ReSe₂ flakes on the HOPG support. The sketch identifies the different regions; (b) an AFM phase image of the region indicated by the dashed box in (a). The arrows indicate the paths used for the AFM step height measurements; (c)-(e) AFM measurements of the step height (a) from HOPG to monolayer; (b) from monolayer to bilayer, and (c) from monolayer to trilayer. The AFM step height for one monolayer is consistently of order 0.6 to 0.7 nm (on the larger monolayer, we obtain 0.67 nm, Figure S1) and the step in (e) is 1.6 nm, close to $2 \times 0.67 = 1.34$ nm. Given this and also the Raman data in the main text, we infer a thickness of three layers for this region.

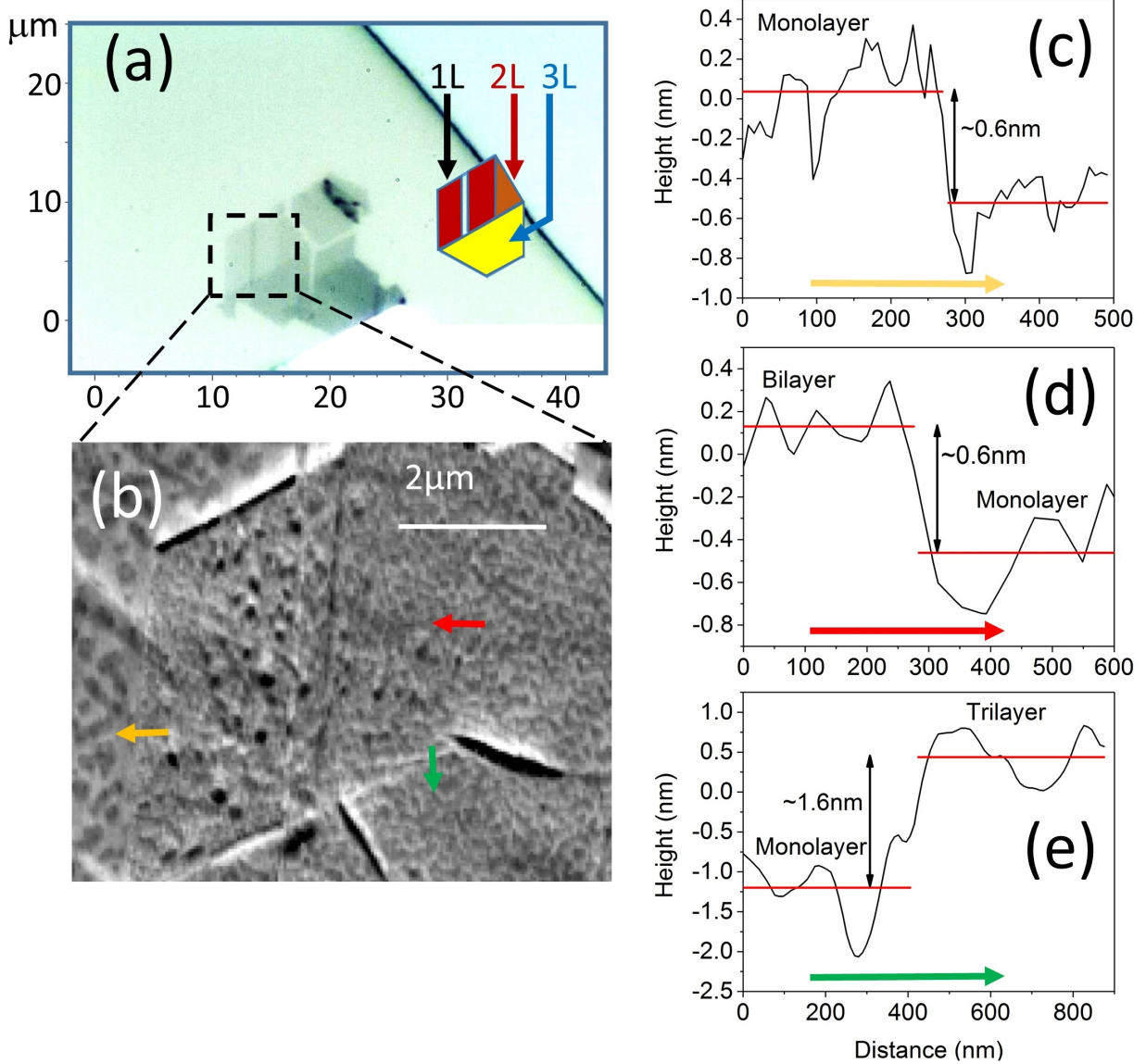


FIG. S3. Photoemission energy distribution curves (EDCs) for monolayer ReSe_2 with momentum in the $\Gamma - M$ direction (left) and the $\Gamma - K$ direction (right); the EDC for Γ is the lower highlighted trace in blue in each case. The vertical dashed lines for $\Gamma - K$ (right) at binding energies of ~ 0.75 (long blue dashes) and ~ 0.88 eV (short red dashes) are guides to the eye, marking estimates of the binding energy at which the photoemission signal rises above the baseline at the Γ and K points respectively; for the $\Gamma - M$ case, left hand side, the blue dashed line at a binding energy of ~ 1.0 eV shows the position in energy of the nearly flat valence band edge.

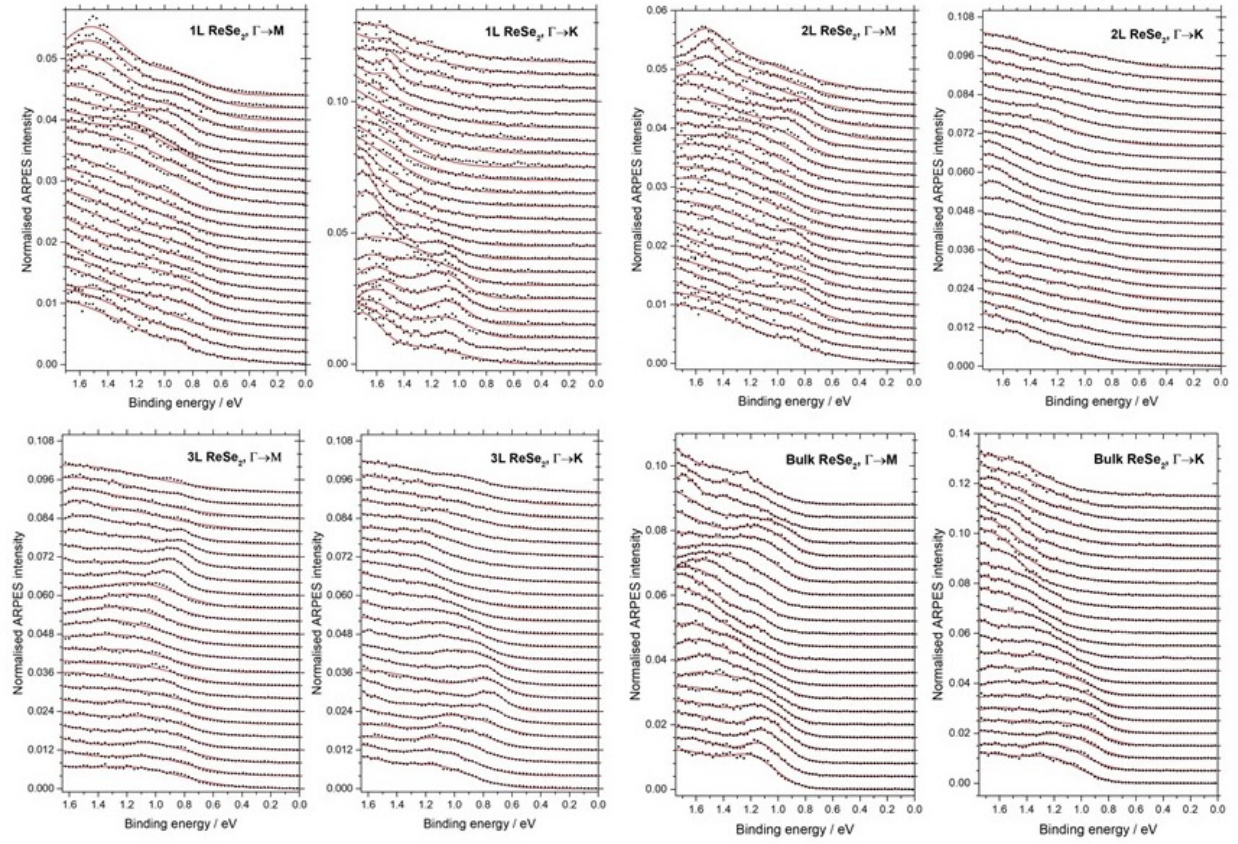


FIG. S4. Photoemission energy distribution curves (EDCs) and fits to them for 1L, 2L 3L and bulk ReSe_2 in the directions $\Gamma - M$ and $\Gamma - K$ as indicated on the top right hand corner of each plot.

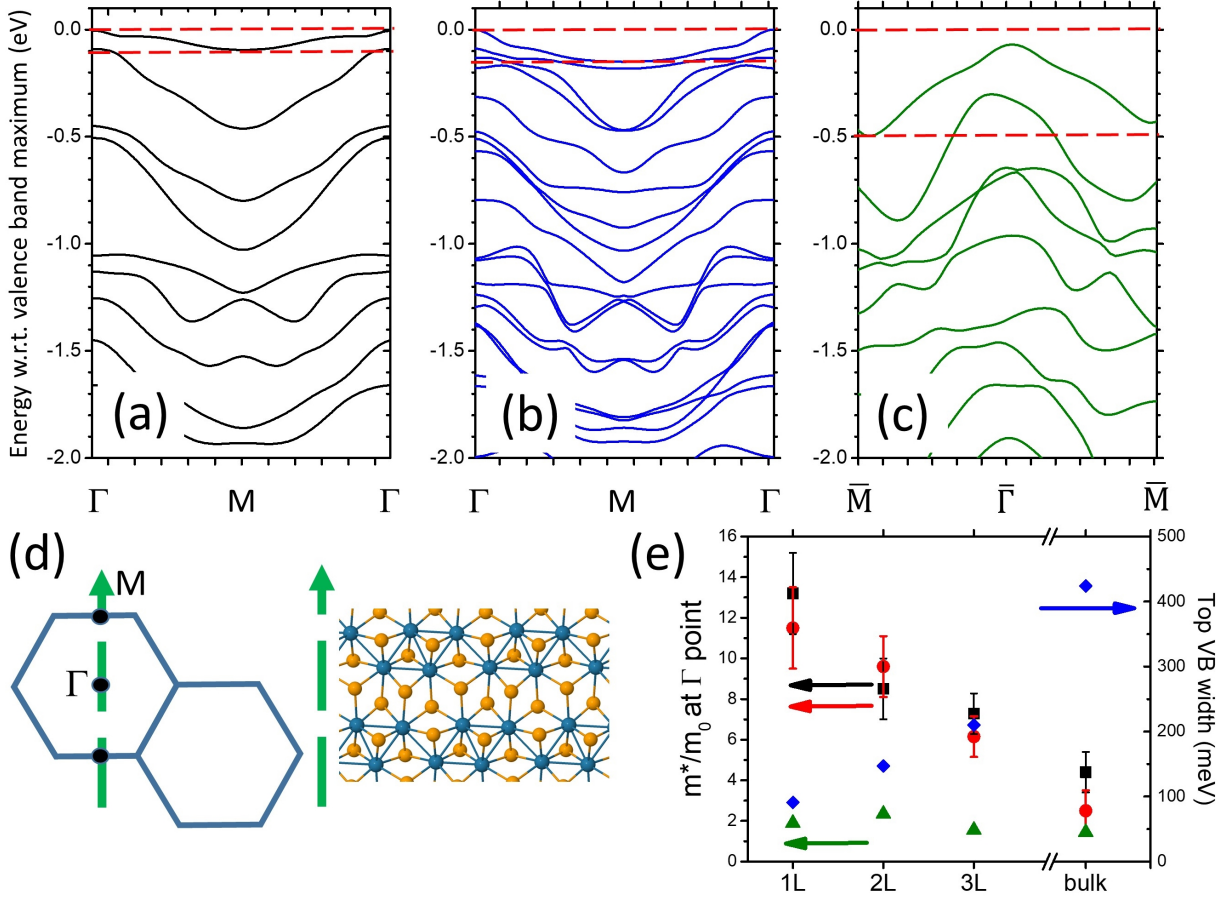


FIG. S5. Calculated dispersions in the $\Gamma - M$ direction for (a) monolayer (1L), (b) bilayer (2L) and (c) bulk ReSe₂ (a section through the 3D Brillouin zone is shown in the case of the bulk material). The dashed red lines show the energies of the top and bottom of the top valence band in each case; (d) the 2D Brillouin zone and in-plane crystal structure of ReSe₂, with the dashed green arrow showing the direction of the momentum slice considered in (a-c).

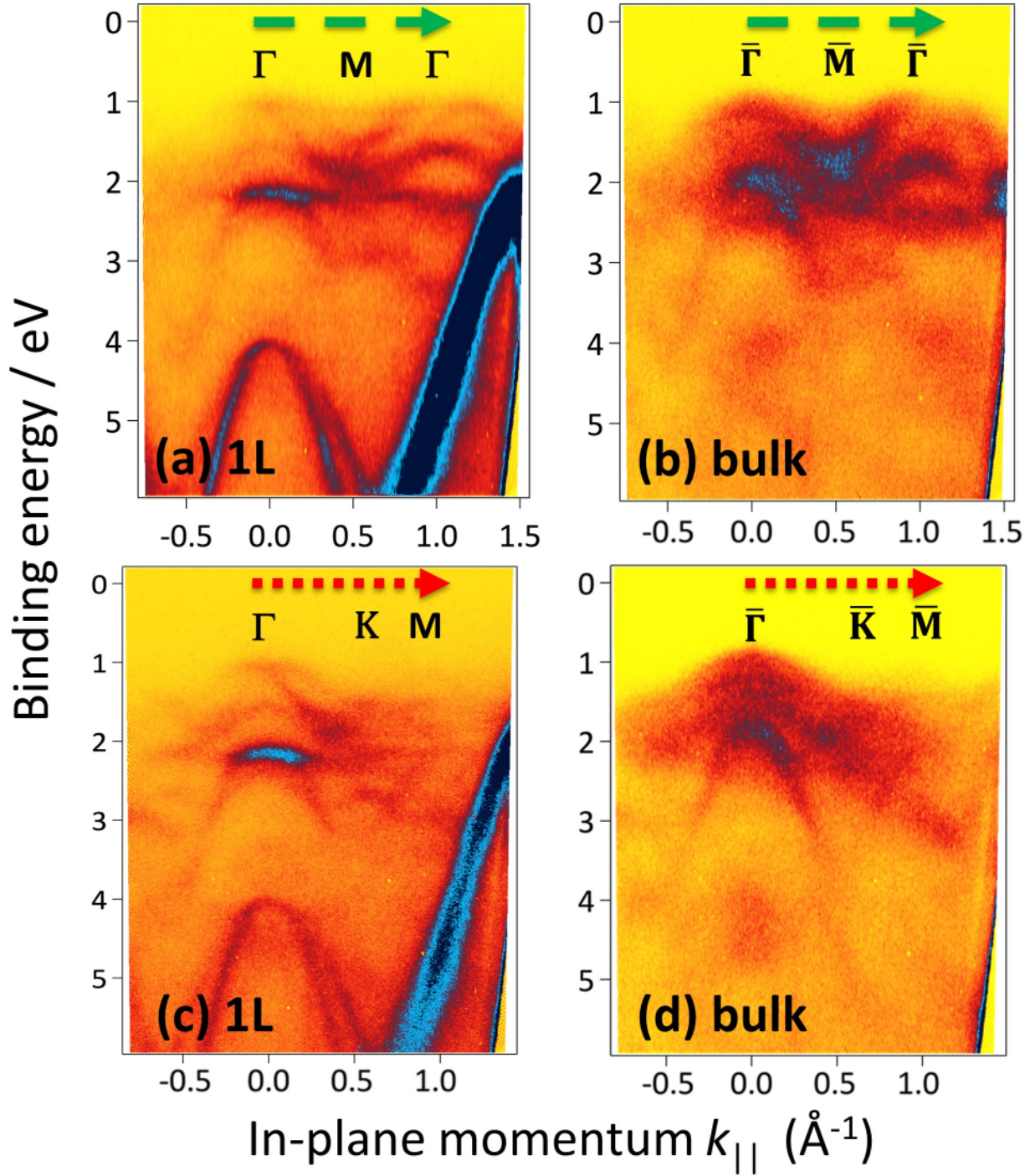


FIG. S6. Comparison of the measured valence band dispersions of a monolayer and a thick bulk flake with identical orientation. (a) and (b): monolayer and bulk dispersions in directions $\Gamma - M$; (c) and (d) monolayer and bulk dispersions in direction $\Gamma - K$.

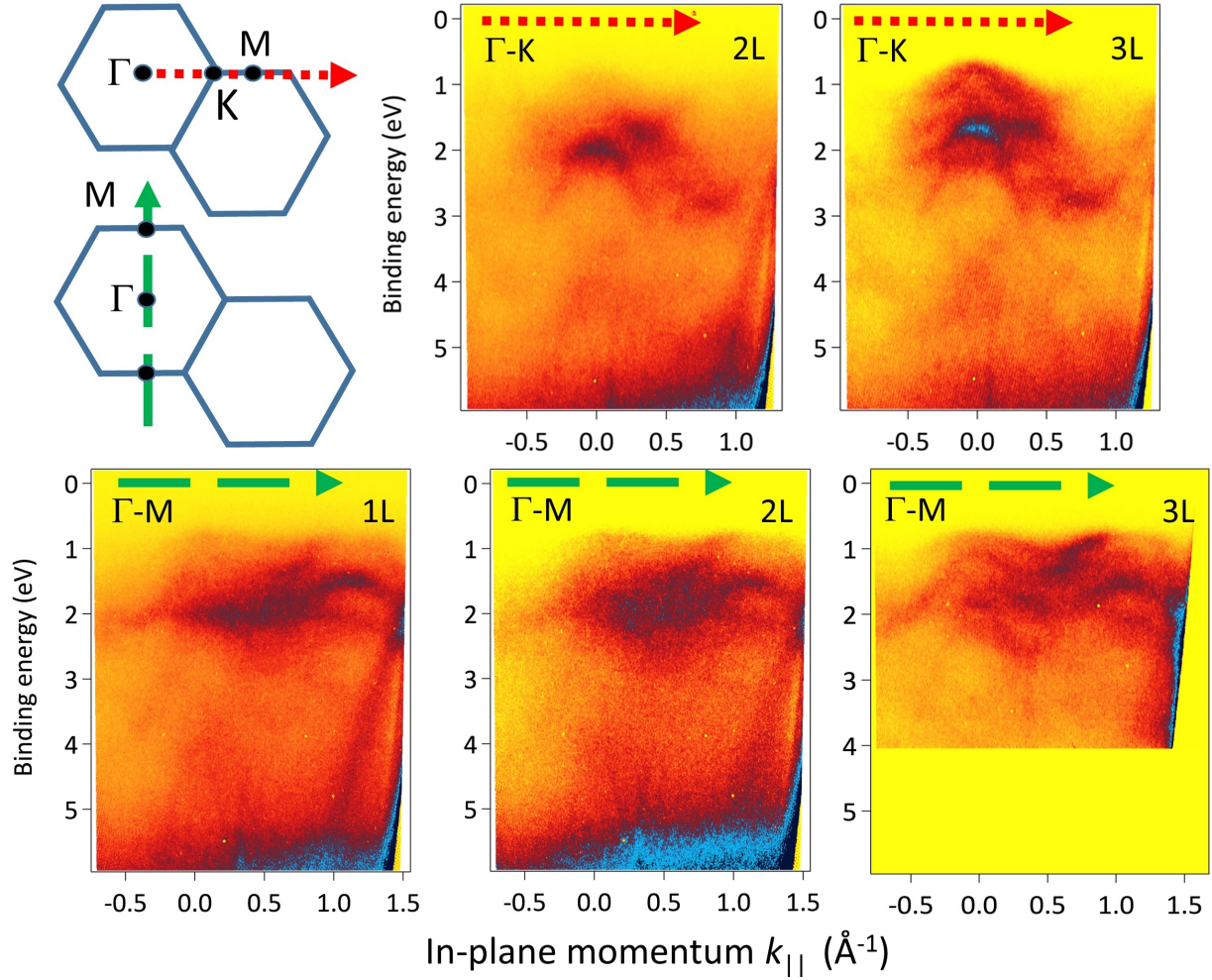


FIG. S7. Comparison of the measured valence band dispersion along directions $\Gamma - K$ (dotted red arrow) and $\Gamma - M$ (dashed green arrow) for mono-, bi- and tri-layer flakes (1L, 2L and 3L), with schematic diagrams of the 2D Brillouin zone used to define the directions of the arrows. The data for $\Gamma - M$ is reproduced from the main paper for comparison. There is no data for $\Gamma - K$ for the 1L region of this sample, but $\Gamma - K$ data is shown for another 1L sample in the main paper.

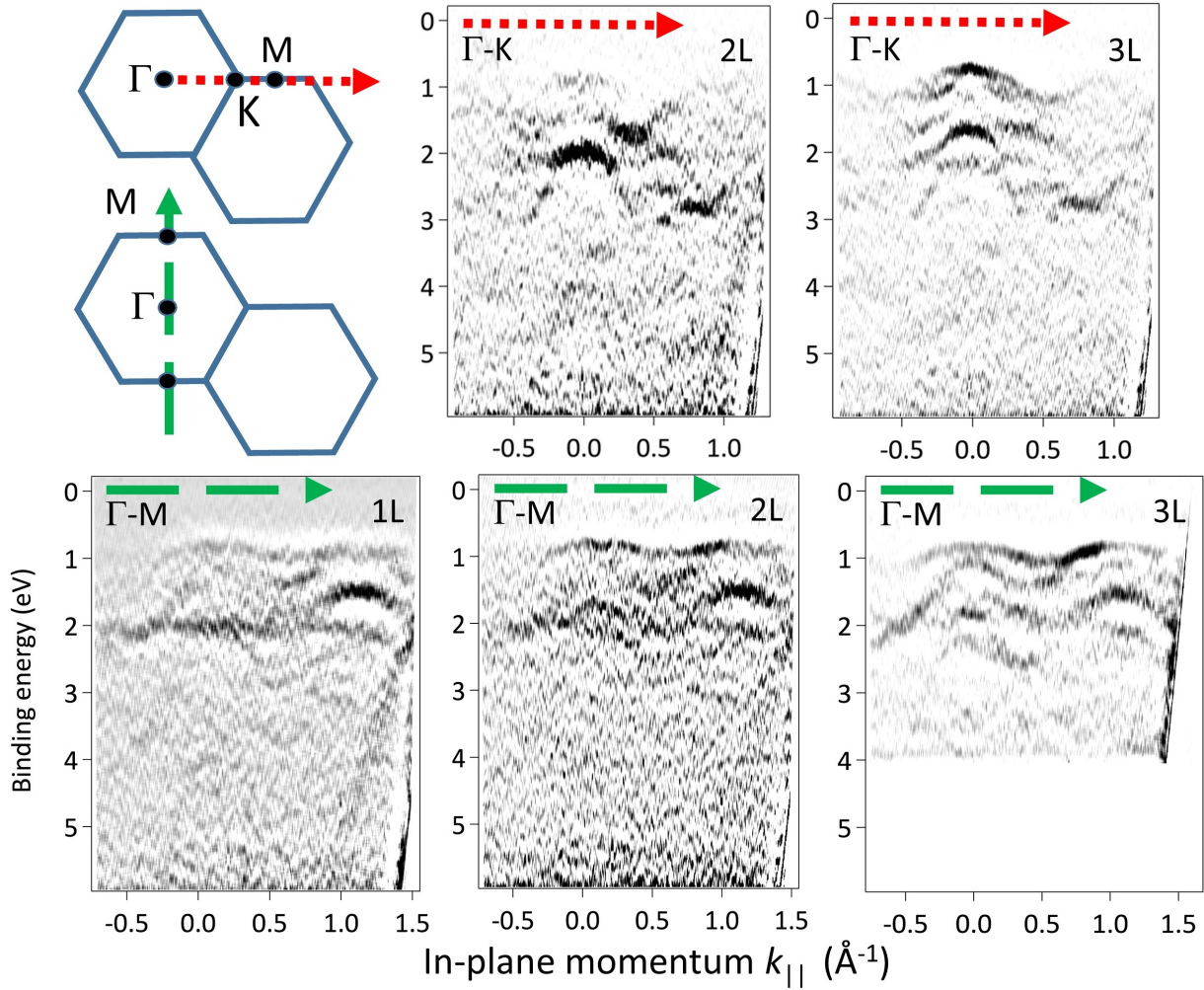


FIG. S8. Comparison of the twice-differentiated valence band dispersion along directions $\Gamma - K$ (dotted red arrow) and $\Gamma - M$ (dashed green arrow) for mono-, bi- and tri-layer flakes (1L, 2L and 3L); the raw data is shown in Figure S5. The trend in the bandwidth extracted from this data is shown in Figure S4.

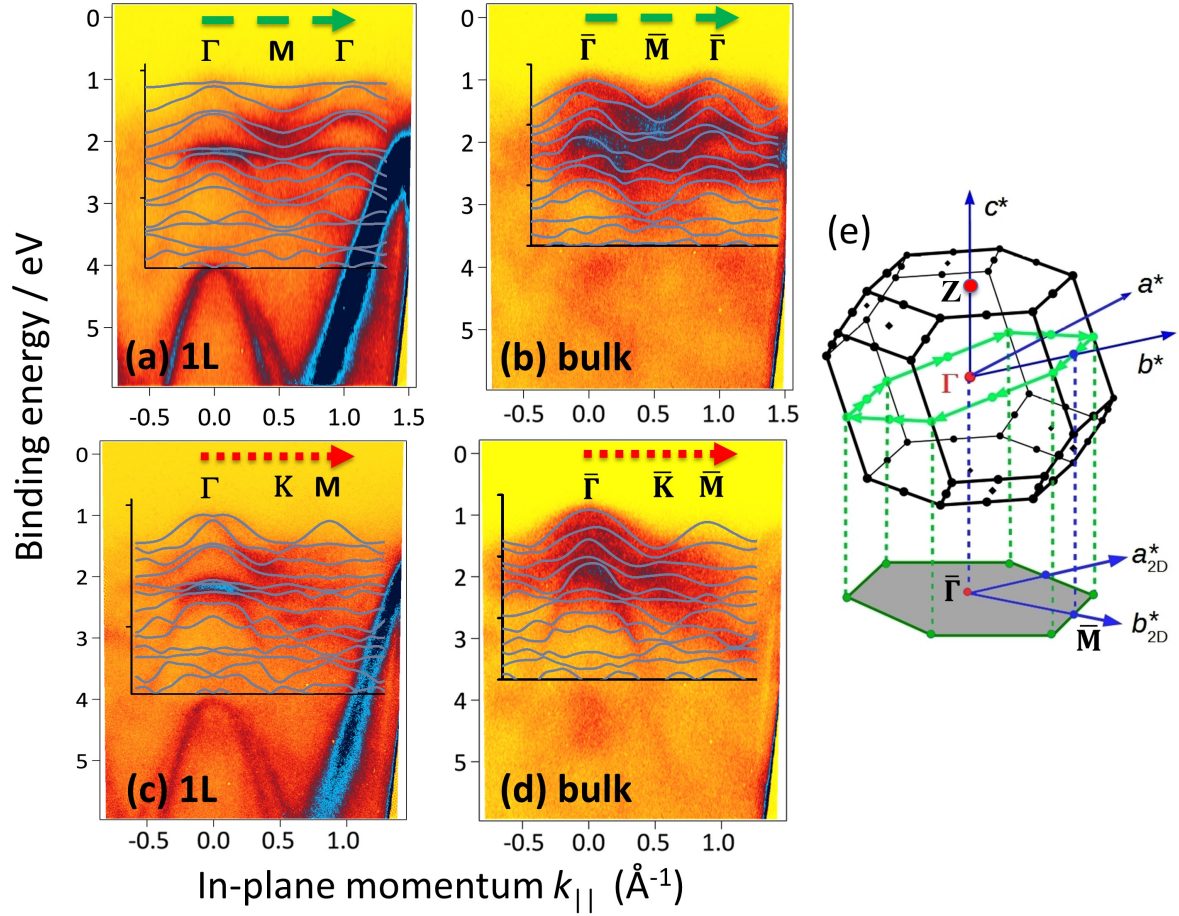


FIG. S9. Comparison of calculated and experimental valence band dispersions of ReSe₂ in the (a,b) $\Gamma - M$ and (c,d) orthogonal $\Gamma - K$ directions for (a,c) monolayer and (b,d) a bulk-like thick flake. The experimental orientations of the bulk and monolayer flakes were identical (they were adjacent on the substrate after exfoliation). (e) shows the bulk 3D and monolayer 2D Brillouin zones with the projected \bar{K} and \bar{M} directions indicated in the latter. The calculations for the bulk dispersion took into account the dependence of k_z on the in-plane momentum using an inner potential of 19 eV [3, 4] and the excitation photon energy of 100 eV. At this energy, we expect to probe the VB near the Z point [3, 5] indicated in (e). Here, fully-relativistic projector augmented wave (PAW) pseudopotentials were used in the LDA approximation in both 1L and bulk cases.

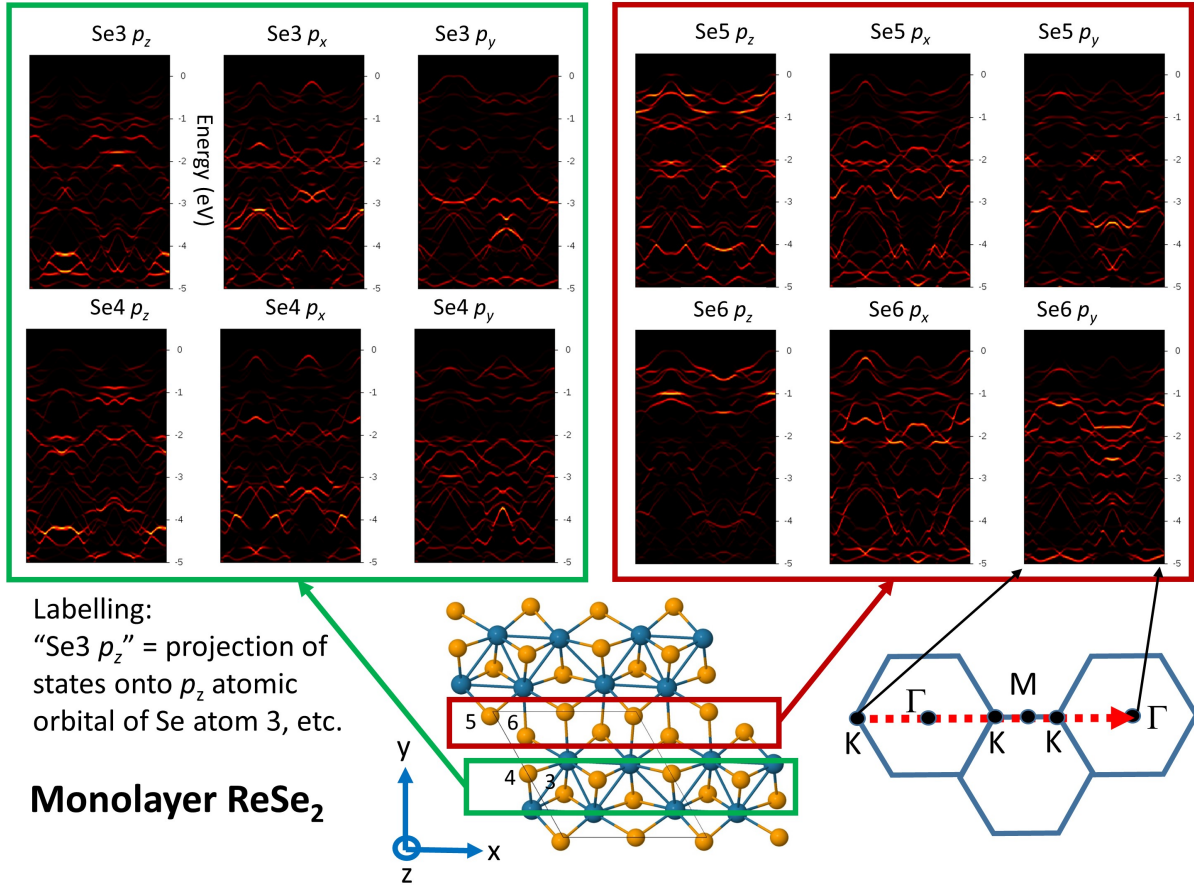


FIG. S10. Calculated valence band dispersion of monolayer ReSe₂ along the direction $\Gamma - K$ projected onto atomic orbitals of Se (calculations here used the scalar-relativistic GGA approximation without spin-orbit interaction, in order to facilitate projection onto atomic states labeled only by orbital angular momentum). The top of the valence band is defined as the zero of energy. Left hand panel (green box): p_z, p_x, p_y states (left to right) of selenium atoms 3 and 4; Right hand panel (red box): projections onto the same states for selenium atoms 5 and 6. The other selenium atoms in the unit cell are related to these four by inversion symmetry. The range of the momentum slice is indicated by reference to the 2D Brillouin zone.

The grouping of the dispersions in Figure S10 highlights the fact that the Se atoms can be assigned to two groups according to their contributions to the valence band structure. The Se atoms (3 and 4) above and below the Re chains have projections which resemble each other much more closely than they do those of atoms 5 and 6 (see, e.g, the p_z contributions near the top of the valence band). This is even more clearly shown in the following, Figure S11,

for the direction $\Gamma - M$.

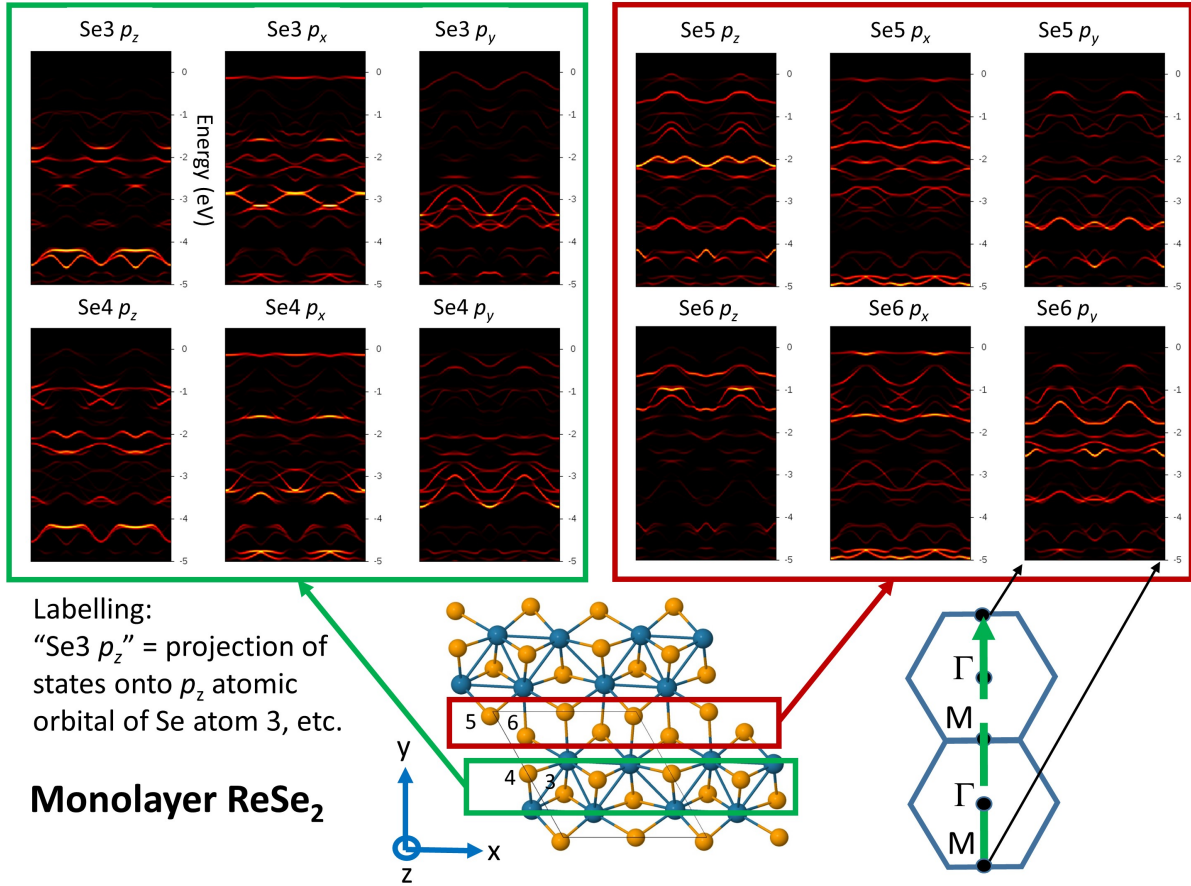


FIG. S11. Calculated valence band dispersion of monolayer ReSe₂ projected onto atomic orbitals of Se, with details as for Figure S8, except that the momentum is now along the orthogonal direction $\Gamma - M$ as indicated with respect to the 2D Brillouin zone (dashed green arrow).

In Figure S11, the very flat band in the $\Gamma - M$ direction is clearly associated with the p_x orbitals of all four Se atoms, especially Se3 p_x and Se4 p_x . Once again, the difference between the contributions of Se atoms 3 and 4 to those of atoms 5 and 6 is clear (see, for example, the dominant contributions of the p_z and p_y states, which are very different).

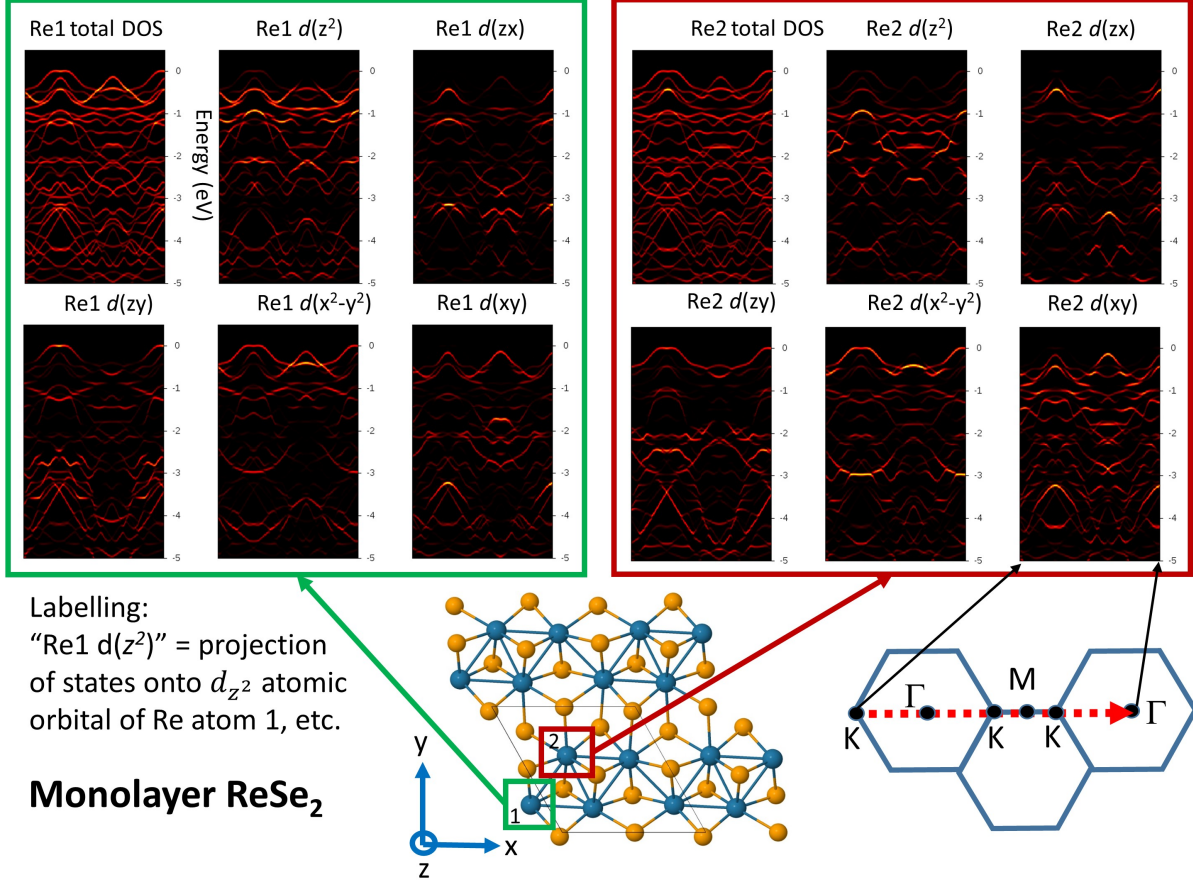


FIG. S12. Calculated valence band dispersion of monolayer ReSe₂ projected onto atomic orbitals of Re, with details as for Figure S8: momentum is along the direction $\Gamma - K$ as indicated with respect to the 2D Brillouin zone (dotted red arrow). Left green box: projections onto d orbitals of Re atom 1; Right red box: projections onto d orbitals of Re atom 2. The other two Re atoms are related to these two by inversion.

Figure S12 shows that, in comparison to the projected states of the Se atoms, the Re atoms at the two non-equivalent sites make similar contributions to the band structure. The compositions of the top valence band near Γ and near K are a key question; unlike many better-known transition metal dichalcogenides, the contribution of Re d_{z^2} at the top of the valence band is small compared to that of Re $d_{x^2-y^2}$ across the whole of the dispersion.

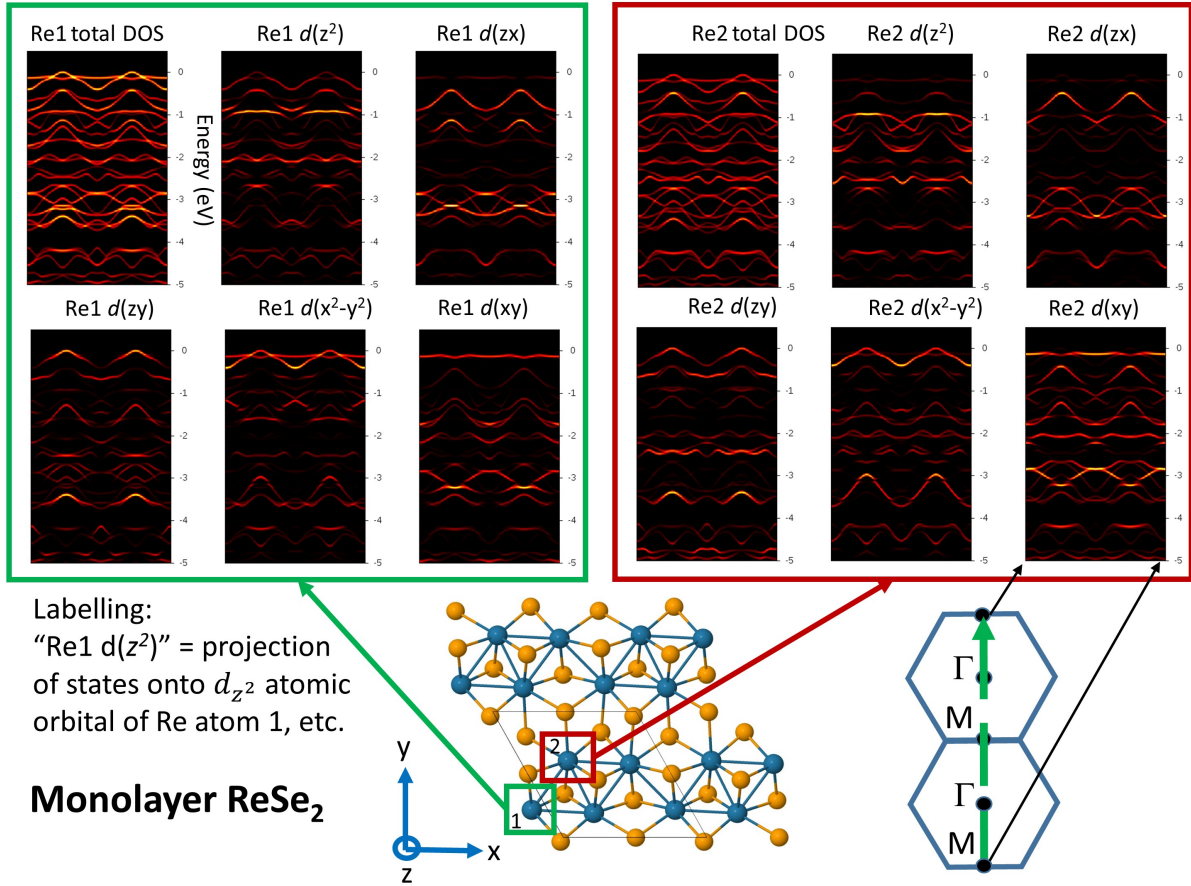


FIG. S13. Calculated valence band dispersion of monolayer ReSe₂ projected onto atomic orbitals of Re, with details as for Figure S8: momentum is along the direction $\Gamma - M$ as indicated with respect to the 2D Brillouin zone (dashed green arrow).

Figure S13 demonstrates that the flat band forming the top of the valence band in the $\Gamma - M$ direction has a strong contribution from the Re $d_{x^2-y^2}$ and d_{xy} states; as in Figure S10, the contribution of d_{z^2} at the top of the valence band is again much smaller. On the other hand, the d_{z^2} states of both Re atoms make a significant contribution near Γ at ~ 1 eV below the top of the valence band; by reference to Figure S7, one can see that these are hybridised principally with Se p_z orbitals. This is the origin of one prominent feature in the experimental ARPES data.

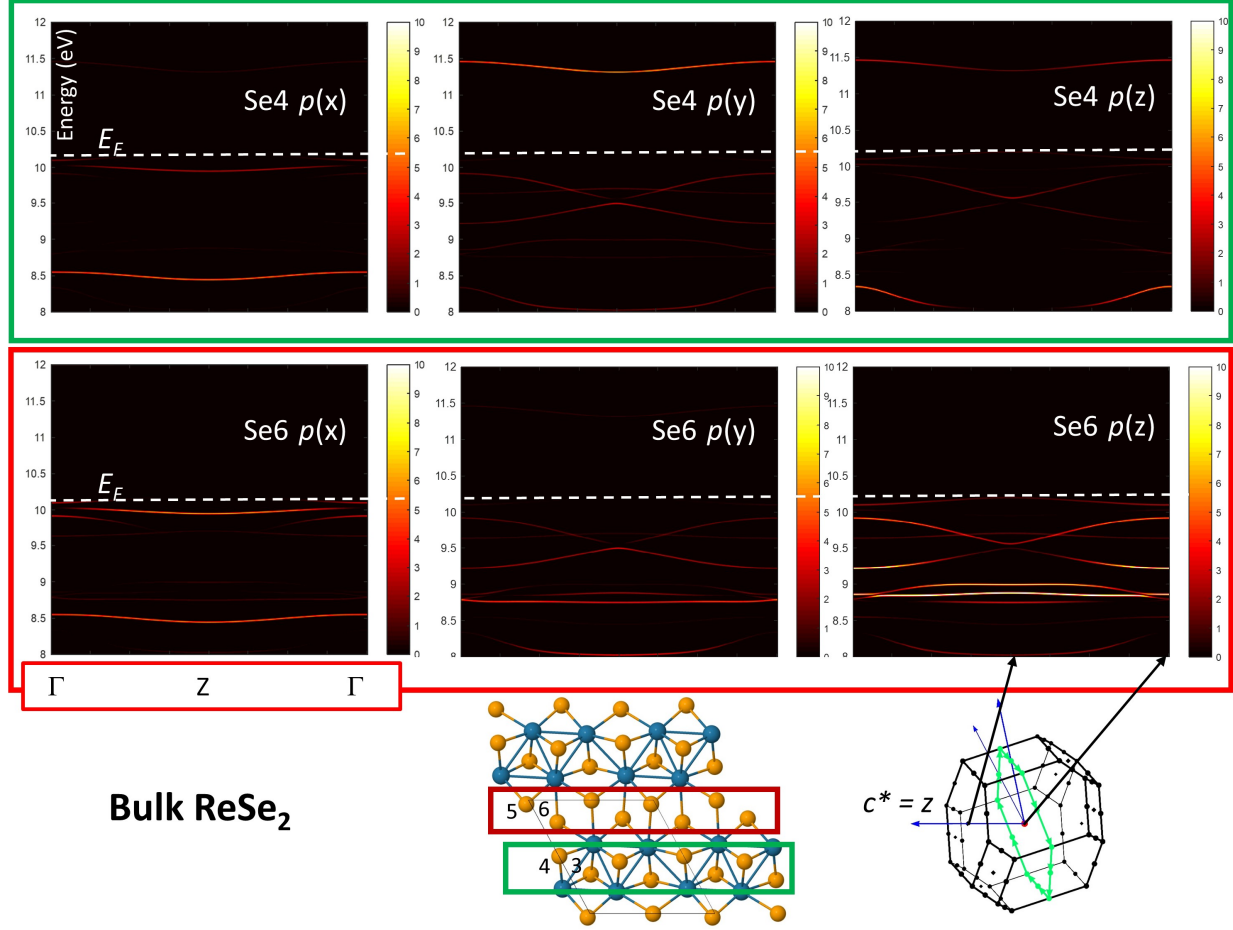


FIG. S14. Calculated dispersion of the valence band of bulk ReSe_2 projected onto atomic orbitals (neglecting spin-orbit effects) for the direction $\Gamma - Z$, perpendicular to the layer planes. Examples of the two types of Se atom are considered (top green box: atom 4; bottom red box: atom 6); the other two atoms (3 and 5) give similar results. The energy of the top of the valence band is indicated by the white dashed lines.

Similar to other DFT-based calculations and experimental data for bulk ReSe_2 , [3–7] we find that the Z point is highest in energy along this path in reciprocal space, as shown in Figure S14. The chalcogen contribution to the uppermost band switches between dominant p_z character at Z to p_x at Γ and both lie very close in energy. In the next figure, SS15, the contributions of the Re atoms to the same bands are analyzed.

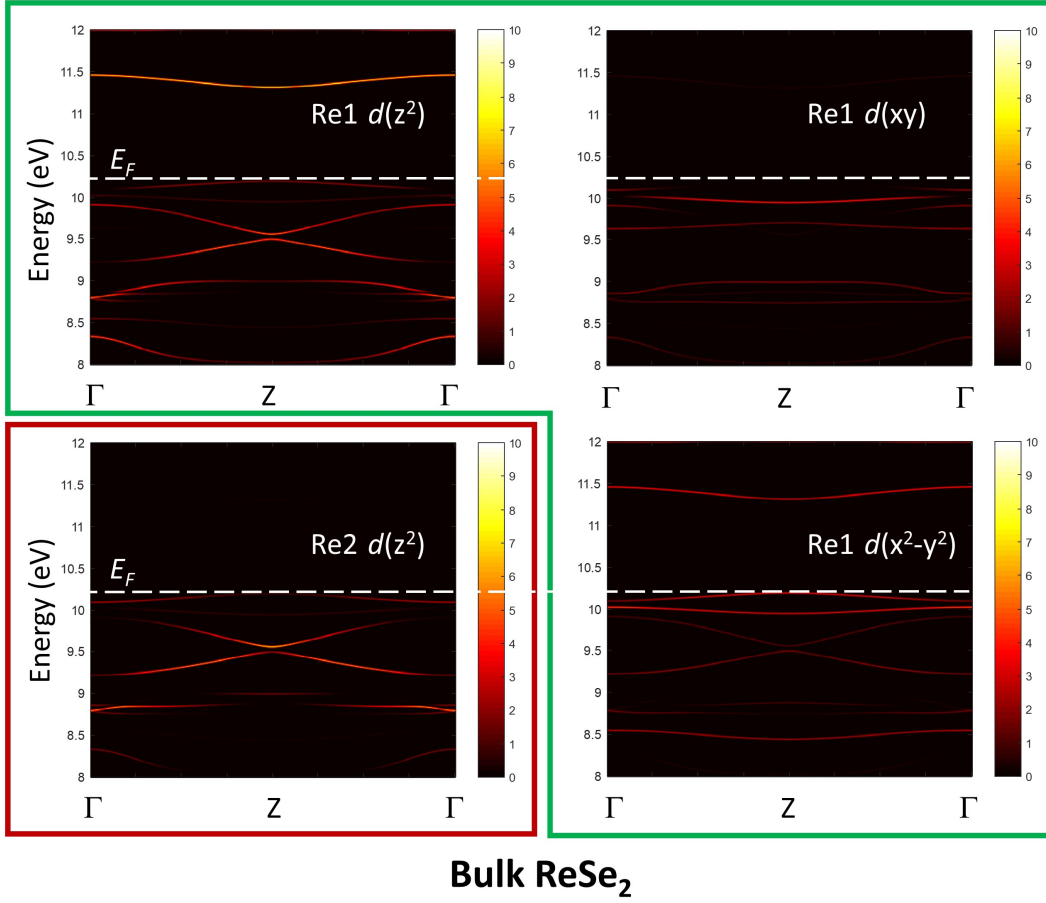


FIG. S15. Calculated dispersion of the valence band of bulk ReSe₂ projected onto atomic orbitals (neglecting spin-orbit coupling) for the direction $\Gamma - Z$, perpendicular to the layer planes, as for Figure S10. The two types of Re atom are considered (top green box: atom 1; bottom red box: atom 2). The energy of the top of the valence band is indicated by the white dashed lines.

Figure S15 shows that the contributions of the Re1 $d_{x^2-y^2}$ and d_{z^2} states to the uppermost valence band are similar in magnitude, and the changes in composition of the top band on moving from Z to Γ are only slight.

-
- [1] A. Castellanos-Gomez, M. Buscema, R. Molenaar, V. Singh, L. Janssen, H. S. Van Der Zant, and G. A. Steele, Deterministic transfer of two-dimensional materials by all-dry viscoelastic stamping, *2D Materials* **1**, 011002 (2014).
- [2] N. R. Wilson, P. V. Nguyen, K. Seyler, P. Rivera, A. J. Marsden, Z. P. L. Laker, G. C. Constantinescu, V. Kandyba, A. Barinov, N. D. M. Hine, X. Xu, and D. H. Cobden, Determination of band offsets, hybridization, and exciton binding in 2D semiconductor heterostructures, *Science Advances* **3**, e1601832 (2017).
- [3] L. S. Hart, J. L. Webb, S. Dale, S. J. Bending, M. Mucha-Kruczynski, D. Wolverson, C. Chen, J. Avila, and M. C. Asensio, Electronic bandstructure and van der waals coupling of ReSe₂ revealed by high-resolution angle-resolved photoemission spectroscopy, *Scientific Reports* **7**, 5145 (2017).
- [4] P. Eickholt, J. Noky, E. Schwier, K. Shimada, K. Miyamoto, T. Okuda, C. Datzler, M. Drüppel, P. Krüger, M. Rohlfing, and M. Donath, Location of the valence band maximum in the band structure of anisotropic 1T'-ReSe₂, *Physical Review B* **97**, 165130 (2018).
- [5] B. S. Kim, W. S. Kyung, J. D. Denlinger, C. Kim, and S. R. Park, Strong one-dimensional characteristics of hole-carriers in ReS₂ and ReSe₂, *Scientific Reports* **9**, 2730 (2019).
- [6] A. Arora, J. Noky, M. Drüppel, B. Jariwala, T. Deilmann, R. Schneider, R. Schmidt, O. Del Pozo-Zamudio, T. Stiehm, A. Bhattacharya, P. Krüger, S. M. de Vasconcellos, M. Rohlfing, and R. Bratschitsch, Highly anisotropic in-plane excitons in atomically thin and bulklike 1T'-ReSe₂, *Nano Letters* **17**, 3202 (2017).
- [7] J. Echeverry and I. Gerber, Theoretical investigations of the anisotropic optical properties of distorted 1T-ReS₂ and ReSe₂ monolayers, bilayers, and in the bulk limit, *Physical Review B* **97**, 075123 (2018).